Journal of The Electrochemical Society, 2020 **167** 124517

Improved Redox Cycling Durability in Alternative Ni Alloy-Based SOFC Anodes

Yusuke Ishibashi,[1] Kohei Matsumoto,[1] Shotaro Futamura,[1] Yuya Tachikawa,[2,3,*] Junko Matsuda,[4,5] Stephen M. Lyth,[4,6] Yusuke Shiratori,[1,2,3,5] Shunsuke Taniguchi,[2,3,5] and Kazunari Sasaki[1,2,3,4,5,6,*,z]

[1]*Department of Hydrogen Energy Systems, Faculty of Engineering, Kyushu University, Nishi-ku, Fukuoka 819-0395, Japan*
[2]*Center of Coevolutionary Research for Sustainable Communities, Kyushu University, Nishi-ku, Fukuoka 819-0395, Japan*
[3]*Next-Generation Fuel Cell Research Center (NEXT-FC), Kyushu University, Nishi-ku, Fukuoka 819-0395, Japan*
[4]*International Institute for Carbon-Neutral Energy Research (WPI-I2CNER), Kyushu University, Nishi-ku, Fukuoka 819-0395, Japan*
[5]*International Research Center for Hydrogen Energy, Kyushu University, Nishi-ku, Fukuoka 819-0395, Japan*
[6]*Platform of Inter/Transdisciplinary Energy Research (Q-PIT), Kyushu University, Nishi-ku, Fukuoka 819-0395, Japan*

Repeated reduction and oxidation of metallic nickel in the anodes of solid oxide fuel cell (SOFC) causes volume changes and agglomeration. This disrupts the electron conducting network, resulting in deterioration of the electrochemical performance. It is therefore desirable to develop more robust anodes with high redox stability. Here, new cermet anodes are developed, based on nickel alloyed with Co, Fe, and/or Cr. The stable phases of these different alloys are calculated for oxidizing and reducing conditions, and their electrochemical characteristics are evaluated. Whilst alloying causes a slight decrease in power generation efficiency, the Ni-alloy based anodes have significantly improved redox cycle durability. Microstructural observation reveals that alloying results in the formation of a dense oxide film on the surface of the catalyst particle (e.g. Co-oxide or a complex Fe–Ni–Cr oxide). These oxide layers help suppress oxidation of the underlying nickel catalyst particles, preventing oxidation-induced volume changes/agglomeration, and thereby preserving the electron conducting pathways. As such, the use of these alternative Ni-alloy based cermets significantly improves the redox stability of SOFC anodes.
 [DOI: 10.1149/1945-7111/abac87]

Manuscript submitted March 23, 2020; revised manuscript received August 3, 2020. Published August 19, 2020.

Solid oxide fuel cells (SOFCs) are promising electrochemical energy conversion devices which can directly generate electricity from hydrogen or hydrocarbon fuels, without the need for combustion. The operating temperature is typically between 600 °C and 1000 °C, leading to advantages such as high electric conversion efficiency, fuel flexibility, and avoidance of expensive noble metal catalysts.[1–6] Fuel cell units have already been commercialized as residential co-generation systems in Japan, where 300,000 units were installed in total as of November 2019,[7] and an increasing fraction of these are based on SOFC. SOFCs are receiving increasing attention for business and industrial applications world-wide, and they can be combined with e.g. a micro gas turbine for higher power generation efficiency.[6] Moreover, it is reported that even higher efficiency beyond 80% is theoretically possible via multi-stage electrochemical oxidation, and replacement of oxide ion charge carriers (O^{2-}) with protons (H^{+}).[8]

For decades, the Ni cermet has been used in conventional SOFC anodes due to its high performance and low cost. This cermet is a composite of metallic nickel as an electron conductor, and ionic conductors such as stabilized zirconia or ceria. However, redox cycling between Ni and NiO causes changes in the volume, as well as Ni particle aggregation. This leads to a disruption of the electron conducting pathways through the Ni metal phase.[9] It is well known that start-stop operation, emergency shut-down, fuel supply interruption, and fuel starvation can cause degradation of SOFC anodes for these reasons, leading to significant performance degradation.[9–27] Therefore, it is necessary to supply reducing hydrogen-containing gas to maintain a reducing atmosphere in the anode region at a high temperature. Purging the anode with hydrogen or inert nitrogen gas is also often needed during shut-down, and operation at high fuel utilization should be avoided in practical SOFC systems. For widespread commercialization of SOFCs in the future, it is desirable to develop an alternative anode with high redox stability and enhanced robustness.

To help solve these important issues, alternative SOFC anodes have been developed in our research group, by using e.g. strontium titanate ($SrTiO_3$) as an alternative electron-conducting framework.[28–32] $SrTiO_3$ has a perovskite structure with high stability in both oxidizing and reducing atmospheres under SOFC operating conditions. It also exhibits higher electronic conductivity by doping the A-site with foreign cations such as La^{3+}.[28–40] In particular, lanthanum-doped strontium titanate (LST, $Sr_{0.9}La_{0.1}TiO_3$) is a promising alternative SOFC anode material, since it has a comparable thermal expansion coefficient to other SOFC electrolyte materials,[33–35] and high electronic conductivity under SOFC operating conditions.[39] Alternatively, Futamura et al. prepared novel SOFC anodes with high redox cycling durability and comparable power generation performance to conventional anodes under 3%-humidified hydrogen supply, by impregnating noble metal catalyst nanoparticles into the porous electrode framework.[31] While redox stability was improved in these cases, further improvement of the electrochemical characteristics at high fuel utilization is needed. Therefore, alternative anodes with both high electrochemical performance and better durability should be developed.

One strategy for preventing degradation of the cermet could be suppression of Ni catalyst particle oxidation. For example, Inconel 600 and Inconel 601 are widely used Ni-alloys with high resistance to oxidation, due to the formation of a dense protective oxide layer at their surface. Therefore, the use of similar alloys (e.g. containing Co, Fe, and/or Cr) could lead to improved redox cycling stability by preventing extensive oxidation of the porous Ni network. Whilst the electrical conductivity of pure metals may be expected to decrease by alloying (since doped atoms can act as scattering sites against electronic transport),[41] we have already shown that power generation characteristics comparable to conventional Ni-cermet anodes can be achieved by alloying.[42]

The aim of this study is to develop robust SOFC anodes for flexible power generation systems. High redox stability without necessitating the use of inert or reducing gases will simplify the

*Electrochemical Society Member.
[z]E-mail: sasaki@mech.kyushu-u.ac.jp

system control of SOFCs. Furthermore, SOFCs with high redox durability can operate at higher fuel utilization. In this work, we first calculate the thermochemical stability of Ni–Co, Ni–Fe, Ni–Cr, and Ni–Fe–Cr alloys. Then, novel cermet anodes comprising nickel alloyed with Co, Fe, and Cr transition metals are prepared. Their electrochemical performance and durability against redox cycling are then evaluated, and they are extensively characterized. The results are used to provide a strategy for improving SOFC performance and robustness via novel Ni-cermet design.

Experimental

Thermochemical equilibrium calculations.—The stability of transition metal elements used in the Ni-alloy based cermet anodes was evaluated by thermochemical equilibrium calculations, using HSC Chemistry software (Version 9.0.5, Outokumpu Research Oy, Finland). The "Reaction Equations" module of this software was applied, for which thermochemical parameters of: NiO (s);[43] CoO (s);[44] Fe_3O_4 (s);[45,46] Cr_2O_3 (s);[47] and H_2O (g)[43,48] were used to calculate the equilibrium oxygen partial pressure with their pure analogues: Ni (s); Co (s); Fe (s); Cr (s); and H_2 (g), between 700 °C and 900 °C. Phase diagrams were obtained by thermochemical calculations using FactSage software (Version 7.4, Thermfact Ltd., Canada) to identify thermochemically-stable compounds in both reducing and oxidizing atmospheres at 800 °C, i.e. a typical operating temperature of SOFCs.

Cell fabrication.—SOFCs with different Ni-alloy based cermet anodes were prepared. Scandia-stabilized zirconia (ScSZ) plates (10 mol% Sc_2O_3–1 mol% CeO_2–89 mol% ZrO_2, Daiichi Kigenso Kagaku Kogyo Co., Ltd., Japan) with a diameter of 20 mm and a thickness of 200 μm were used as solid electrolytes. Anode powders were prepared by mixing Ni-containing metal oxides and gadolinium-doped ceria (GDC, Rhodia, ULSA grade, USA) in a ratio of 48.1:51.9 by weight, corresponding to a volume ratio of 50:50 (assuming that the metal oxide composite powder was pure NiO). GDC was used as a mixed ionic electronic conductor. The Ni-containing metal oxides were prepared by the ammonia co-precipitation method, as shown schematically in Fig. 1. In this procedure, a precipitate of metal hydroxides was obtained by dropping aqueous ammonia into an aqueous solution of Ni ions, and the alloying element ions. Then the precipitated Ni-containing metal oxides and hydroxides were collected by filtration, followed by heat treatment. In the ammonia co-precipitation method, an aqueous solution containing various ions is generally dropped directly into aqueous ammonia. However, if Ni ions are directly added into aqueous ammonia, a Ni complex can form. To prevent this, aqueous ammonia was added into aqueous solution. Lanthanum strontium manganite (LSM, $(La_{0.8}Sr_{0.2})_{0.98}MnO_3$, Praxair, USA) was applied as the cathode material. The cathode paste for the functional layer was made with LSM and ScSZ powder in a 50:50 ratio by weight. The current-collecting cathode layer comprised LSM powder.[27,31,32]

The cell structure is shown schematically in Fig. 2a. Porous anode layers were screen-printed onto the ScSZ electrolyte plates, followed by sintering in air at 1300 °C for 3 h. Cathode layers were then screen-printed onto the counter side of the ScSZ electrolyte plates, followed by sintering in air at 1200 °C for 5 h. A reference electrode with a geometric area of ca. 0.04 cm^2 was then painted ca. 2 mm away from the edge of the cathode, using Pt paste in order to separate overvoltages on the anode side and on the cathode side. Pt mesh (80 mesh acting) was attached to each electrode surface as a current collector. The thickness of the electrode layers was approximately 40 μm, and the geometric area was 8 by 8 mm^2 (0.64 cm^2).

Cell performance test.—Figure 2b shows the electrochemical experimental setup. Before measuring the electrochemical characteristics, the cell was heated up to 1000 °C at 200 °C h^{-1}, in order to melt the Pyrex glass ring and to seal the cell. 3%-humidified H_2 gas was then supplied to the anode for 1 h at 100 ml min^{-1}, in order to reduce the Ni-containing metal oxide to Ni-based alloy or related compounds. The overall I-V characteristics, anodic nonohmic overvoltage, and anode-side ohmic (IR) loss, were measured at 800 °C utilizing 3%-humidified hydrogen gas. The gas flow rates of pure hydrogen and air to the anode and the cathode were 97 and 150 ml min^{-1}, respectively. The anode-side voltage losses (i.e. the voltage between the anode and the reference electrode on the cathode side) were separated into anodic non-ohmic and ohmic overvoltages using the well-known current

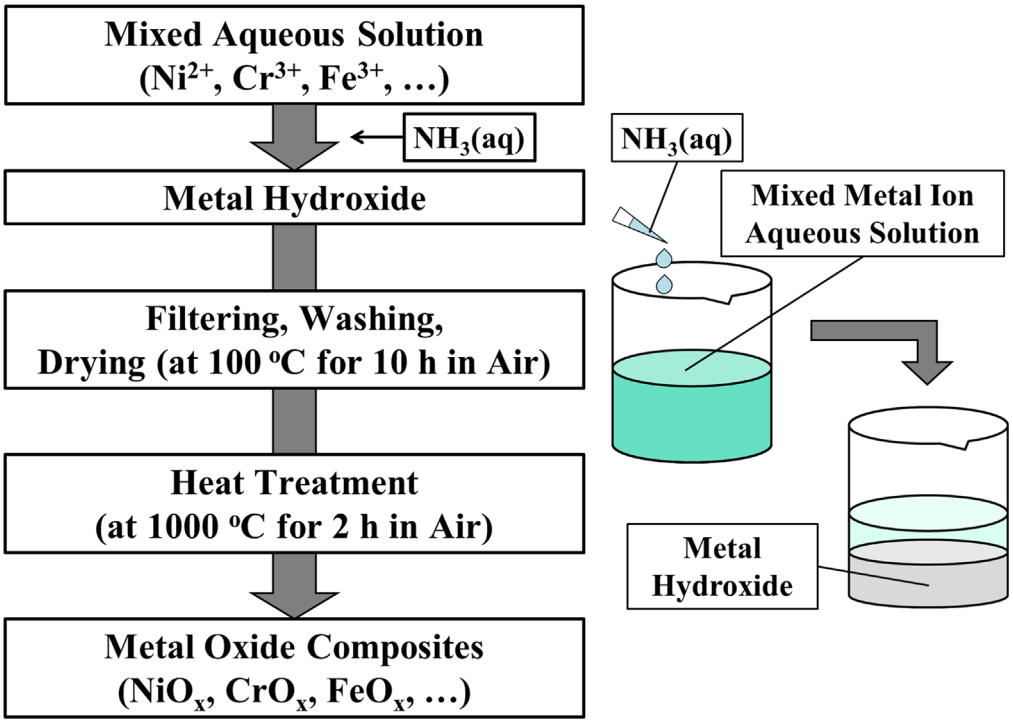

Figure 1. Preparation procedure of metal oxide composite powders by the ammonia co-precipitation method.

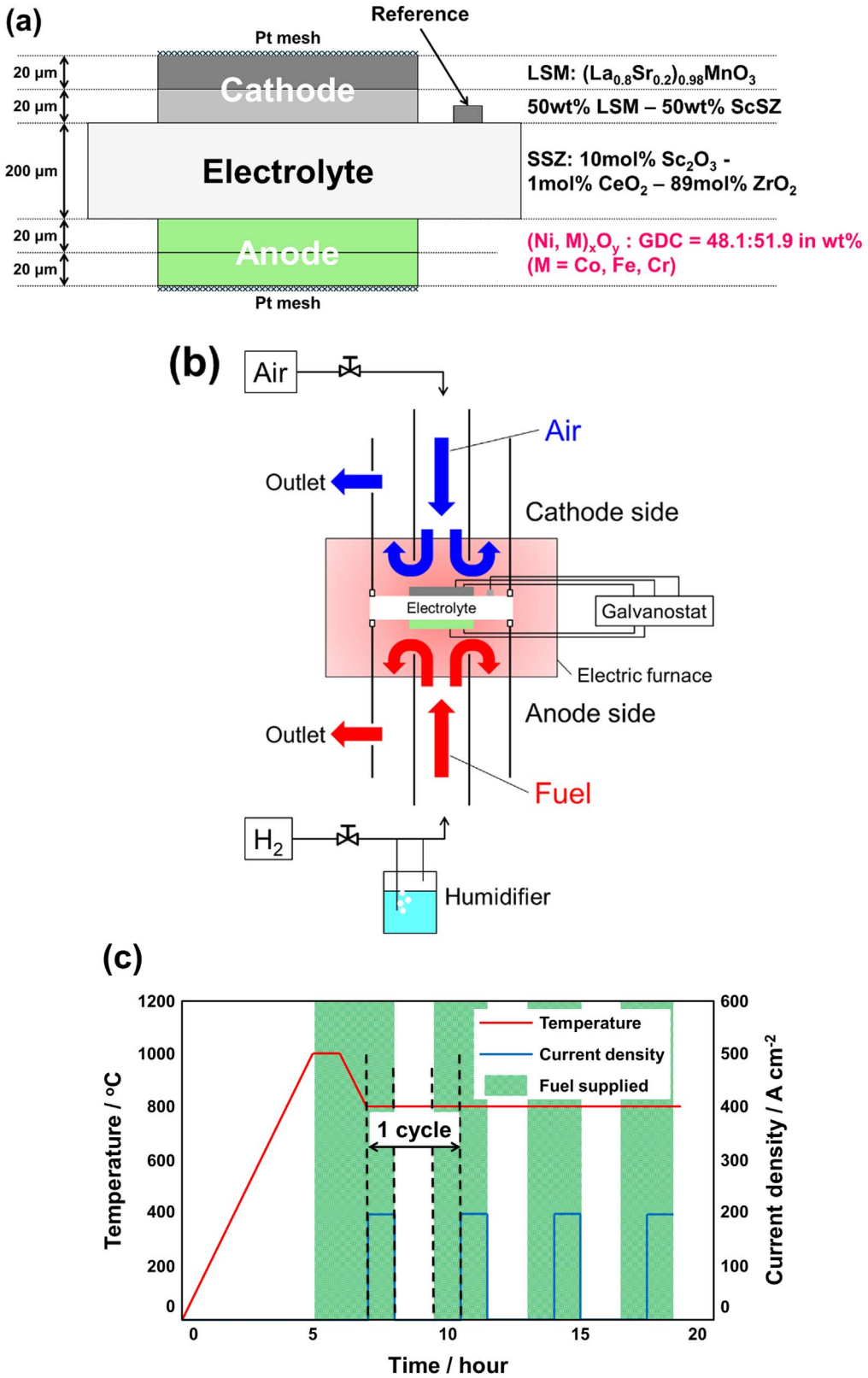

Figure 2. Schematic drawings of: (a) the SOFC single cell used in this study; (b) the experimental setup for the electrochemical measurements; and (c) the protocol applied in redox cycling tests (The flow rate of 3%-humidified hydrogen fuel: 100 ml min^{-1}).[25]

interruption method.[27,31,32,49] The cathode-side voltage losses (i.e. the voltage between the cathode and the reference electrode on the cathode side) were also separated into cathodic non-ohmic and ohmic overvoltages using this method. It should be noted that the position of the equipotential surface of the reference electrode can shift if the anode and the cathode are not perfectly aligned, shifting the reference potential from the midpoint of the electrolyte plate.[50,51] Such effects cannot be practically excluded in testing of real fuel cell systems. Therefore, to confirm the reproducibility of the anode-side ohmic losses and anodic overvoltage, representative

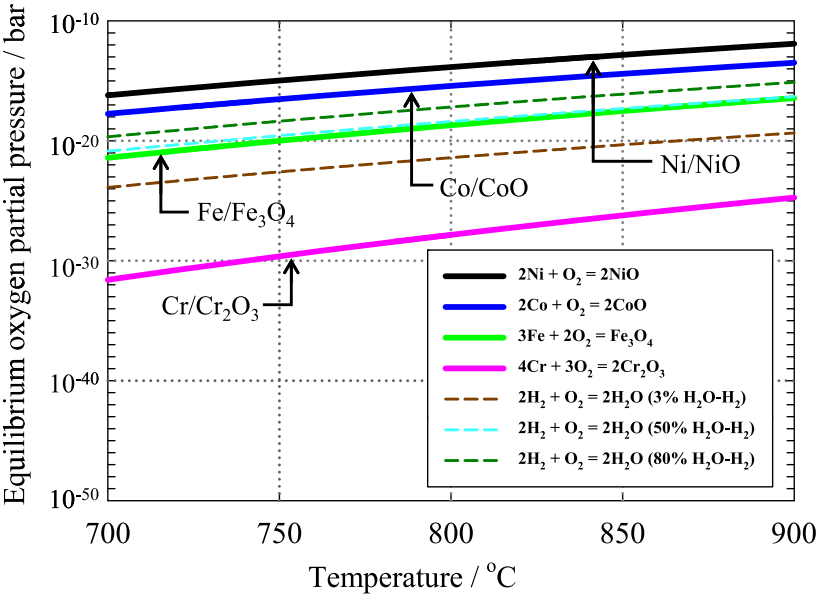

Figure 3. Thermochemical stability diagram for Ni, Co, Fe, and Cr. The co-existence $p(O_2)$ boundaries of these metals and their oxides are shown by solid lines as a function of temperature. The oxygen partial pressure of humidified hydrogen gases is also shown by dashed lines for comparison.

data after electrochemical measurements using two to four different cells were analyzed. In contrast, the cell voltage (which also incorporates cathode and electrolyte overvoltages) is not affected by this issue.

Redox cycling test.—Redox cycling tests were conducted following a protocol based on shutdown tests simulating practical SOFC systems as shown in Fig. 2c, as previously performed by Hanasaki et al.[27] In this shutdown cycle test, we focused on fuel supply interruption, which is the major cause of Ni oxidation at the anode. In order to evaluate the degradation related phenomena of SOFCs due to the redox cycles, the cell voltage, the anodic non-ohmic overvoltage, the anode-side ohmic losses, the cathodic non-ohmic overvoltage, and the cathode-side ohmic losses, were measured during the redox cycling tests. The cell was operated with normal fuel supply at a current density of 0.2 A cm^{-2} for 1 h. The fuel supply was then interrupted, and the cell was kept at a constant temperature of 800 °C for 1.5 h. Under these conditions, the residual hydrogen was consumed by ambient air gradually diffusing through the glass seal, resulting in a decrease in the open-circuit cell voltage to < 0.1 V within ca. 20 min, and < 0.01 V within ca. 50 min. The anode environment was thus kept in an oxidizing atmosphere (ambient air and residual water vapor) for >1 h, simulating typical redox cycles in SOFC systems. The fuel supply was then restored, and this process was repeated 50 times. After this, the hydrogen-containing atmosphere on the anode side was substituted with pure nitrogen gas, and cooled after the open-circuit cell voltage reached zero. The nominal cooling rate used in the furnace (ARF-40K, As-one, Japan) was 800 °C h^{-1}, but effectively the cell was cooled naturally near ambient temperature. These procedures prevented major changes in the materials during cooling, but residual water vapor and/or oxygen impurities in the nitrogen gas at the anode could still oxidize the surface.

Microstructural observation.—Cross-sectioning of the anodes and elemental mapping were performed using a focused ion beam-scanning electron microscope (FIB-SEM, Versa 3D Lovac, FEI) combined with energy dispersive X-ray spectroscopy (EDS, EDAX Octan Super, AMETEK). The SEM acceleration voltage was 20 kV, and secondary electron images were taken for the EDS analysis. For FIB-SEM observation, cell samples were infiltrated with an epoxy resin (EpoxiCure™ 2, Buehler) under vacuum conditions, and then cut to the size of the FIB-SEM sample stage.

In order to analyze the distribution of Ni particle sizes in the anode, two-dimensional cross-sectional SEM images of the anode (x-y plane) were collected with a spacing of 30 nm along the z-direction, by a sequential milling and observation using a different FIB-SEM (Helios NanoLab 600i, FEI). The 3D distribution of Ni particles in the middle of the anode layers was reconstructed using computer processing software (Amira, Version 6.3, FEI). Each SEM image had dimensions of 20 μm (x) by 17 μm (y) with a resolution of 1024 by 884 pixels. A volume of ca. 7 μm by 7 μm by 3 μm (z) was evaluated in the anode for the 3D reconstruction. Back-scattered electron images were taken to separate the Ni-containing phases (Ni or Ni-alloy) and Ce-containing phases (GDC) for size analysis, with a lower accelerating voltage of 3 kV.

A transmission electron microscope (TEM, JEM-ARM200F, JEOL, Ltd., Japan) was applied for higher resolution elemental mapping and electron diffraction analysis. Scanning transmission electron microscope (STEM)-EDS revealed microstructural changes and associated elemental redistribution in the anode by redox cycling. Electron diffraction patterns from selected areas in the anode were analyzed to determine their crystallographic phases. Specimens for the TEM/STEM analyses were taken from the epoxy infiltrated and sectioned samples.

Results and Discussion

Stability diagram.—When fuel is supplied to an SOFC anode, the cermet should contain metallic nickel for the electrochemical reactions to proceed efficiently. Meanwhile, when the fuel supply is interrupted, the Ni generally oxidized. Alloyed elements added to try and suppress Ni oxidation should sacrificially oxidize at a lower oxygen partial pressure compared to Ni. This is so that they can form a protective oxide layer around the particle before Ni itself has a chance to oxidize. As such, the elements selected for these alloys should be strategically selected to be stable as metals during power generation, whilst oxidizing before Ni during the stop cycles.

Stability diagrams can predict the oxygen partial pressure at which metals and their oxides can coexist as a function of temperature. Figure 3 shows stability diagrams which plot the phase boundaries of selected metals (Ni, Co, Fe, and Cr) and their oxides, as a function of temperature. The more commonly used Ellingham diagram plots the Gibbs free energy on the vertical axis,[52–54] but the stability diagram shown here uses the equilibrium oxygen partial pressure. Stable metallic phases exist at oxygen partial pressure values below the co-existence boundary, while stable oxide phases exist above the boundary. The oxygen partial pressures at the metal/oxide co-existence boundaries are those expected from the Ellingham diagram.[52–54] Dashed lines show the thermochemically

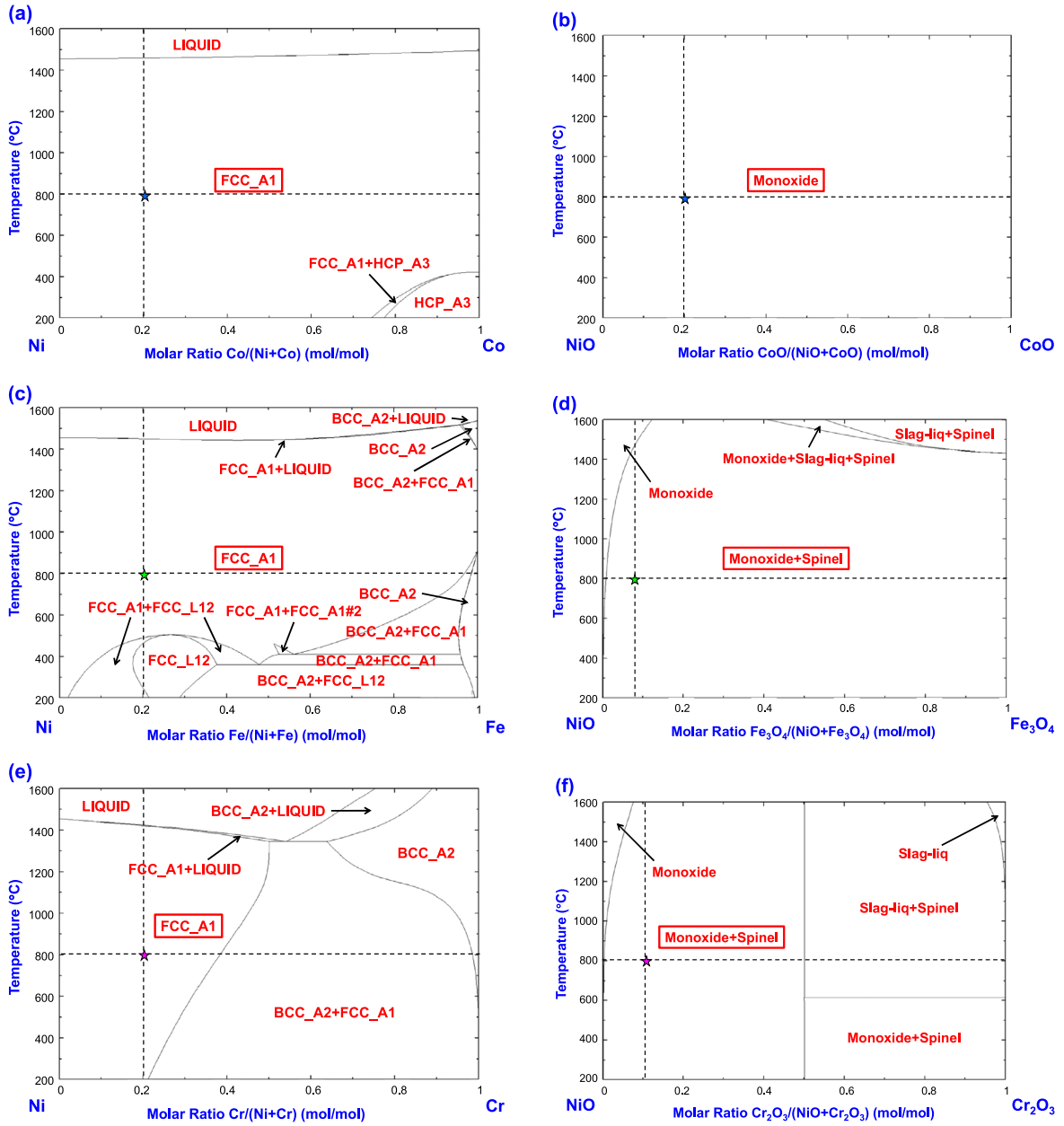

Figure 4. Phase diagrams of nickel with selected elements and their oxides: (a) Ni–Co; (b) NiO–CoO; (c) Ni–Fe; (d) NiO–Fe_3O_4; (e) Ni–Cr; (f) NiO–Cr_2O_3; (g), (i) Ni–Cr–Fe; and (h), (j) NiO–Cr_2O_3–Fe_3O_4. Calculations were performed for ambient pressure, and the temperature for the ternary phase diagrams is fixed at 800 °C. A1, A2 etc. are symbols for the classification of crystal structure types, obtained from the Strukturbericht designation and structure reports.[56] Pure metals of Cu, W and Mg are representatives of A1, A2, and A3, respectively. The crystal structure of Ni has the same fcc structure as that of Cu and A1. Cu_3Au is one of ordered alloys, which is a representative of L12.

calculated oxygen partial pressure of hydrogen-based fuels at different humidification levels (3%, 50%, and 80%), which are consistent with those independently calculated using equilibrium constants between 700 °C and 900 °C, derived from the Gibbs energy of formation of H_2O (g) (–194.2 kJ mol^{-1} at 700 °C, and –183.1 kJ mol^{-1} at 900 °C).[55]

It is clear from these calculations that in this case the most easily oxidized element is Cr. The equilibrium oxygen partial pressure of Cr/Cr_2O_3 is lower than that of Ni/NiO by ca. 15 orders of magnitude. The co-existence oxygen partial pressure boundary of Cr/Cr_2O_3 is lower than that of typical humidified hydrogen fuels, so this element is expected to form a stable oxide even when reducing hydrogen fuel is supplied. The co-existence oxygen partial pressure boundary of Fe/Fe_3O_4 is also lower than that of highly humidified hydrogen fuels, so that iron will be oxidized when hydrogen fuel humidified beyond 50% is supplied (i.e. at a high fuel utilization). In contrast, the co-existence boundary of Co/CoO is located just below that of Ni/NiO. This suggests that Co will be in the metallic phase within a wide humidification range even beyond 80% (i.e. up to a high fuel utilization beyond ca. 80%) during SOFC operation, but will be oxidized before metallic Ni when fuel supply is interrupted, as thermochemically expected in Fig. 3.

Phase diagrams.—Phase diagrams were calculated to determine whether these elements can form alloys with Ni, or if they will form other unwanted phases. Figure 4 shows the binary and ternary phase diagrams calculated for reducing conditions (metallic phases) and oxidizing conditions (oxide phases). Crystallographic structures were allocated based on the Strukturbericht designation and structure reports.[56] The vertical dashed lines represent the chemical

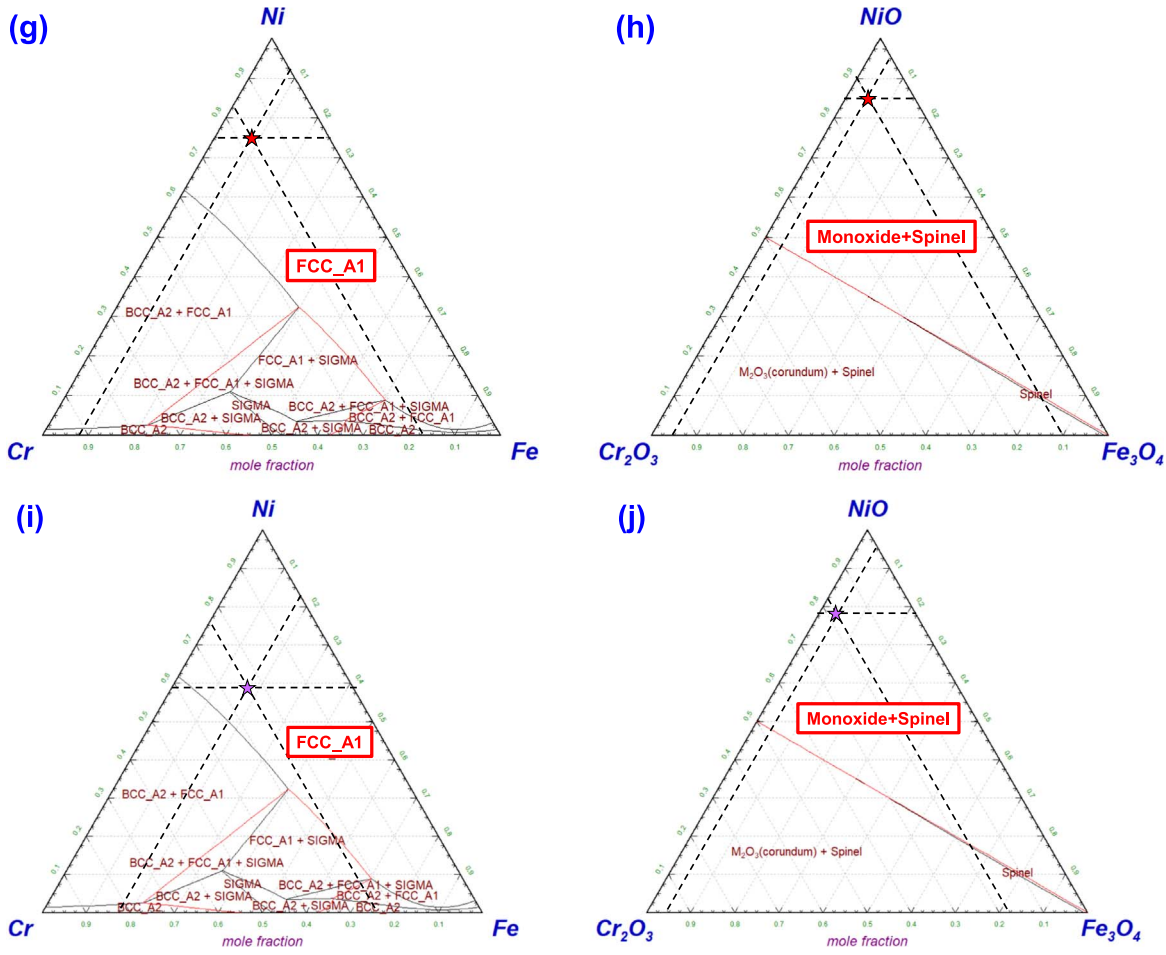

Figure 4. (Continued.)

composition of the prepared materials (e.g. 80:20 mol% for the binary alloys), and the horizonal dashed lines represent SOFC operation temperature (i.e. 800 °C in this study). The intersection of these dashed lines (highlighted with a star) represents the experimental conditions of this study. The stable phases under these conditions are highlighted with a red square in the phase diagrams. The stable phases of ternary alloys with composition similar to Inconel 600 and Inconel 601 are also shown.

Figure 4a shows that Ni–Co alloys with fcc structure are stable under reducing conditions, over a wide composition range. Under oxidizing conditions, a solid solution of NiO and CoO will be formed (Fig. 4b). Similarly, Ni–Fe alloys with fcc structure are stable under reducing conditions (Fig. 4c). However, under oxidizing conditions, the Ni–Fe alloy will separate into NiO (monoxide) and Fe_3O_4 spinel (Fig. 4d) phases. Meanwhile, Ni–Cr alloys will form a single fcc phase under reducing conditions (Fig. 4e), whilst under oxidizing conditions they will form NiO (monoxide) and $NiCr_2O_4$ spinel (Fig. 4f) phases. However, it should be noted that Cr is likely to form a stable oxide rather than alloying with Ni (Fig. 3). As such, synthesized Ni–Cr alloys are expected to consist mainly of Ni with a small amount of dissolved Cr, and a significant proportion of Cr oxide, even under reducing conditions (i.e. when humidified hydrogen fuel is supplied).

Figures 4g to 4j show ternary phase diagrams for Ni–Cr–Fe alloys. According to these, single-phase Ni–Cr–Fe alloy with fcc structure is stable under fully reduced conditions, separating into NiO and a mixed $(Ni/Cr/Fe)_3O_4$ oxide with spinel structure upon oxidation. However, in practice, Ni–Cr–Fe cermet anodes likely comprise not only the Ni–Cr–Fe metallic alloy, but also of Cr-oxide (corundum-type) and Fe-oxide (spinel-type) due to the relatively high stability of these phases even under reducing fuel supply conditions (see Fig. 3).

I–V characteristics and overvoltages.—SOFCs with Ni-alloy based cermet anodes were prepared. The molar ratios of the Ni and alloyed metals are depicted as subscripts. The ternary alloy compositions were designed to mimic Inconel 600 and Inconel 601, i.e. $Ni_{74.5}Cr_{17.2}Fe_{8.3}$-GDC and $Ni_{58.3}Cr_{25.0}Fe_{16.7}$-GDC (neglecting other minor elements in Inconel 601). All cells were supplied with 3%-humidified hydrogen fuel in this study. The I–V characteristics of the cells with a conventional Ni-GDC cermet and the Ni-alloy based cermet anodes are shown in Fig. 5a. For the conventional LSM-based cathodes of cells with six different types of anodes, the cathodic non-ohmic overvoltages are shown in Fig. 5b, and the ohmic losses on the cathode side are shown in Fig. 5c. The anodic non-ohmic overvoltages are shown in Fig. 5d, and the ohmic losses on the anode side are shown in Fig. 5e. In Fig. 5, the average values are shown, while their standard deviations are also shown with error bars. The open circuit voltage measured for the 3%-humidified hydrogen fuel at 800 °C in Fig. 5a is that expected from the oxygen partial pressure thermochemically calculated in Fig. 3.

Figures 5b and 5c reveal that the identically-prepared LSM-based cathodes of 15 cells statistically exhibited comparable cathodic overvoltages and cathode-side ohmic losses, even with the different anodes. In fact, the standard deviation of the cathode-side overvoltages (Figs. 5b and 5c) was smaller than the differences in overvoltages on the anode side (Figs. 5d and 5e). As expected, the conventional Ni-GDC anode exhibits the highest initial I–V performance (Fig. 5a). Meanwhile, the $Ni_{80}Co_{20}$-GDC and $Ni_{80}Fe_{20}$-GDC alloy anodes have comparable I–V

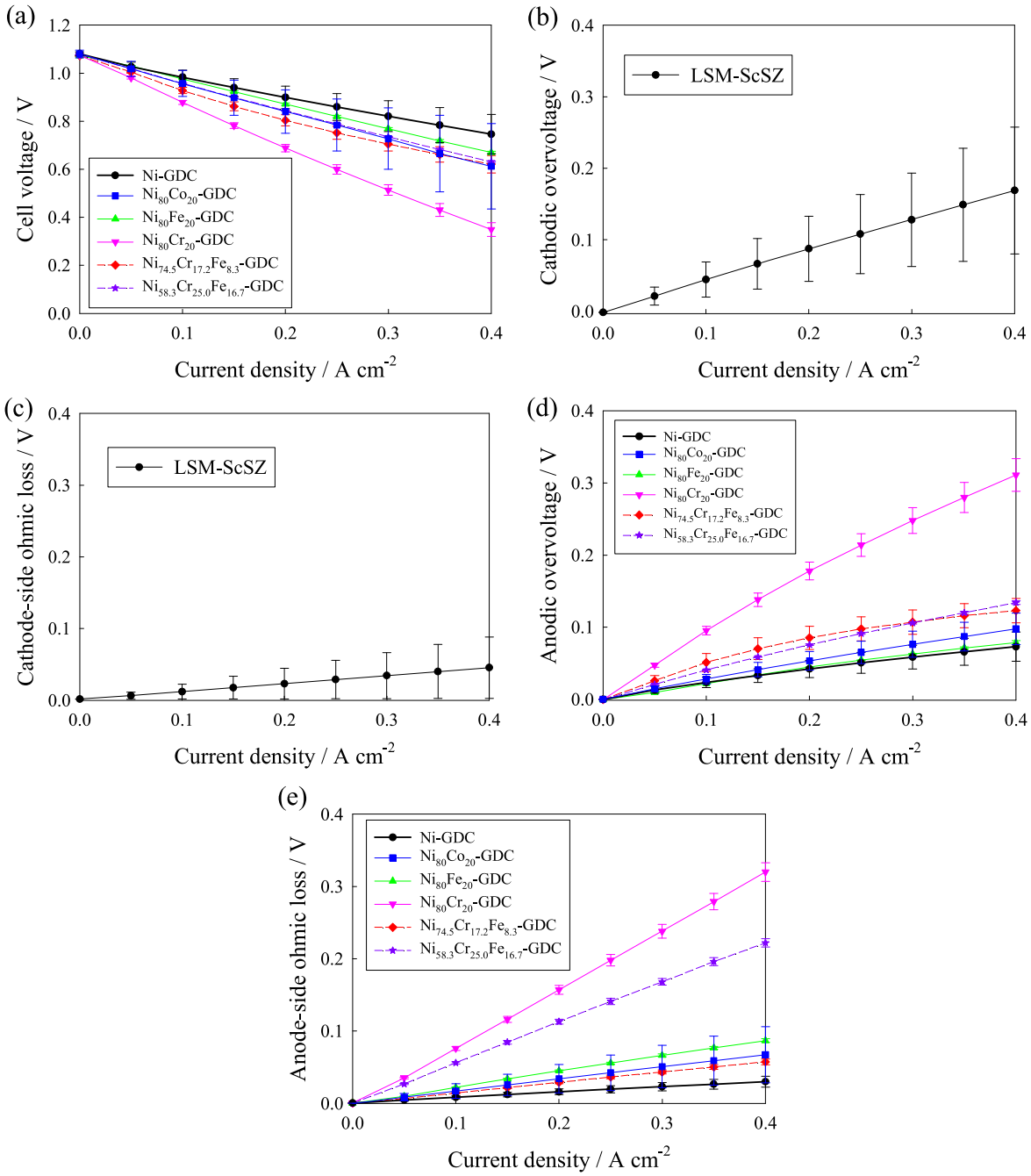

Figure 5. Single cell I–V characteristics (3%-humidified H_2 fuel) for the fabricated anodes: (a) cell voltage; (b) cathodic non-ohmic overvoltage; (c) cathode-side ohmic (IR) losses; (d) anodic non-ohmic overvoltage; and (e) anode-side ohmic losses.

characteristics. This shows that the alloying with Co and Fe does not significantly affect the initial electrochemical performance. The ohmic and non-ohmic overvoltages (Figs. 5d and 5e) on the anode side are also not significantly different from the conventional anode. These results are attributed to the fact that Co and Fe readily alloys with Ni in the presence of 3%-humidified hydrogen fuel (as confirmed in the thermochemical calculations), and that no resistive oxide phases are expected to form under these SOFC operation conditions. A much larger decrease in performance is observed for binary alloy $Ni_{80}Cr_{20}$-GDC, associated with large ohmic and non-ohmic overvoltages. This is attributed to the formation of Cr-oxide phases even under reducing conditions, as predicted in the thermochemical calculations. Such oxide phases evidently increase the resistance of the anode layer (ohmic overvoltage) since they do not well conduct electrons, and potentially block the electrochemical active sites (non-ohmic overvoltage). Similarly, the ternary alloy anodes (dashed lines) also both have relatively lower initial performance, as reflected in the large ohmic and non-ohmic overvoltages. Again, this is attributed to the formation of stable oxide phases, as predicted in the thermochemical calculations.

Redox stability.—The stability of the anodes was investigated by applying 50 redox cycles following the protocol shown in Fig. 2c. The resulting changes in representative cell voltage are shown in Fig. 6a. Figures 6b and 6c show overvoltages on the cathode side. These figures again indicate that the LSM-based cathodes of 15 cells exhibited comparable cathodic overvoltages and cathode-side ohmic losses, which were relatively stable and were not affected by the redox cycling on the anode side, as expected. Conventional Ni cermet anodes display a fairly dramatic decrease in cell voltage

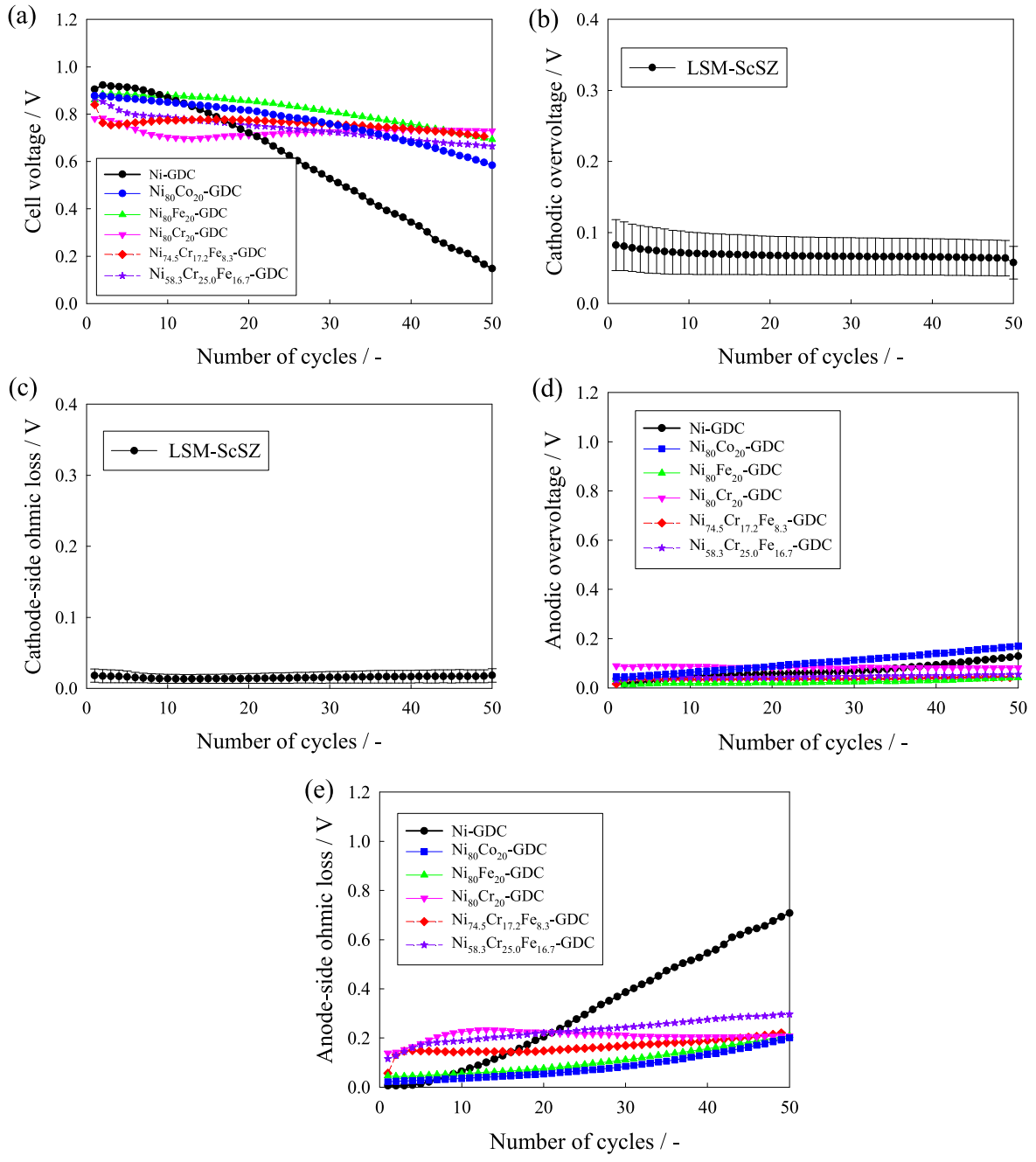

Figure 6. Redox cycling test results (3%-humidified H_2 fuel) for the fabricated anodes: (a) cell voltage; (b) cathodic non-ohmic overvoltage; (c) cathode-side ohmic (IR) losses; (d) anodic non-ohmic overvoltage; and (e) anode-side ohmic losses.

(Fig. 6a), associated with a considerable increase in anode-side ohmic losses (Fig. 6e). In contrast, the cell voltages with the binary and ternary Ni-alloy based anodes are remarkably stable, translating to enhanced SOFC durability. The changes in anodic non-ohmic overvoltage during the cycling tests are small for all of the anodes (Fig. 6d). These results indicate that the catalytic activity of the anodes is not compromised by alloying. Meanwhile, the ohmic losses increase considerably in the conventional Ni cermet anode during cycling (Fig. 6e). This is probably due to destruction of the electron-conducting pathways due to Ni particle aggregation,[25] leading to increased resistance. The Ni-alloy anodes undergo a much more gradual increase in ohmic losses, indicating that oxidation-induced degradation of the electron-conducting network is effectively suppressed in these samples.

Anode microstructure.—FIB-SEM micrographs and the associated EDS Ni intensity maps of the conventional Ni-GDC anode, the $Ni_{80}Co_{20}$-GDC anode, and the $Ni_{74.5}Cr_{17.2}Fe_{8.3}$-GDC anode, before and after redox cycling are shown in Figs. 7–9, respectively. Secondary electron images are shown as the FIB-SEM micrographs in these figures. Aggregation of the Ni catalyst particles is observed in the conventional Ni-GDC anode after redox cycling, especially by comparing Figs. 7c and 7d, in agreement with the increased ohmic resistance seen in Fig. 6e. In contrast, aggregation is not observed in the Ni-alloy based anodes (Figs. 8 and 9). This qualitative comparison of the microstructures confirms that alloying can prevent Ni aggregation.

Quantitative analysis of the microstructure was also performed. The Ni particle size distributions are shown in Fig. 10, obtained from

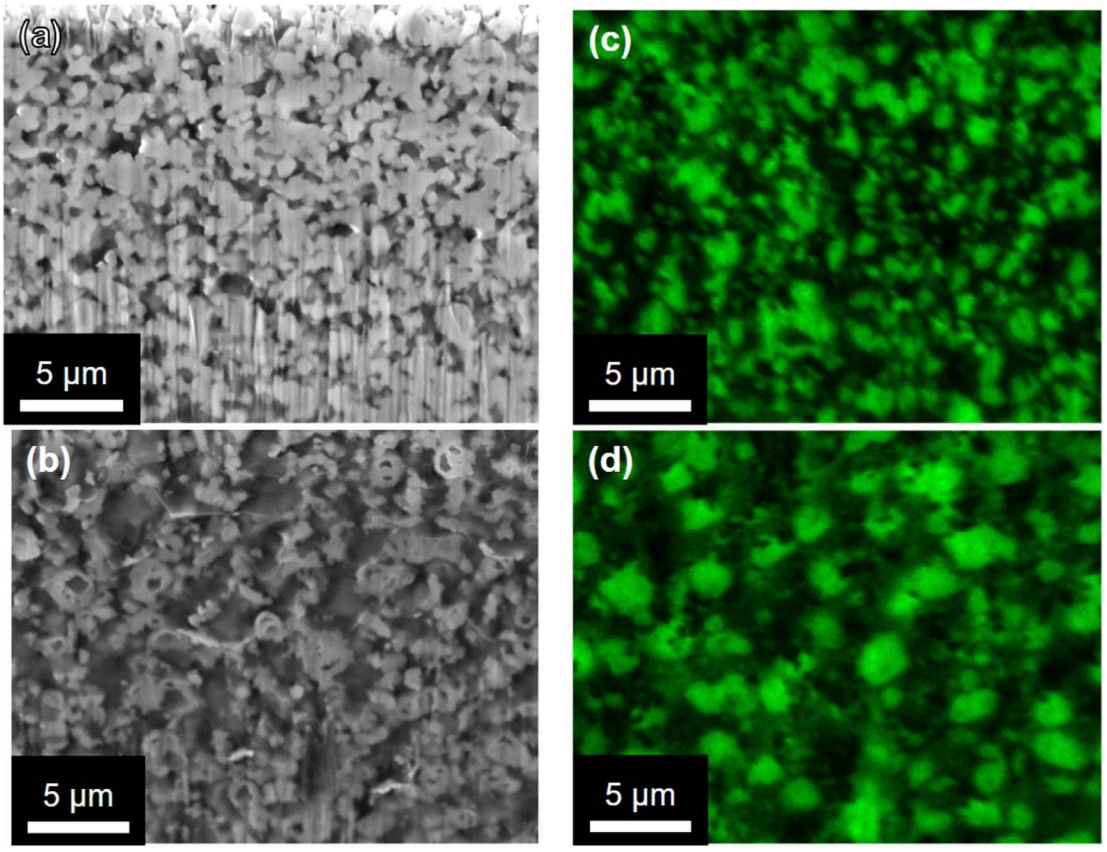

Figure 7. (a), (b) FIB-SEM micrographs, and (c), (d) Ni EDS intensity maps of the Ni-GDC anode: (a), (c) before, and (b), (d) after 50 redox cycles.

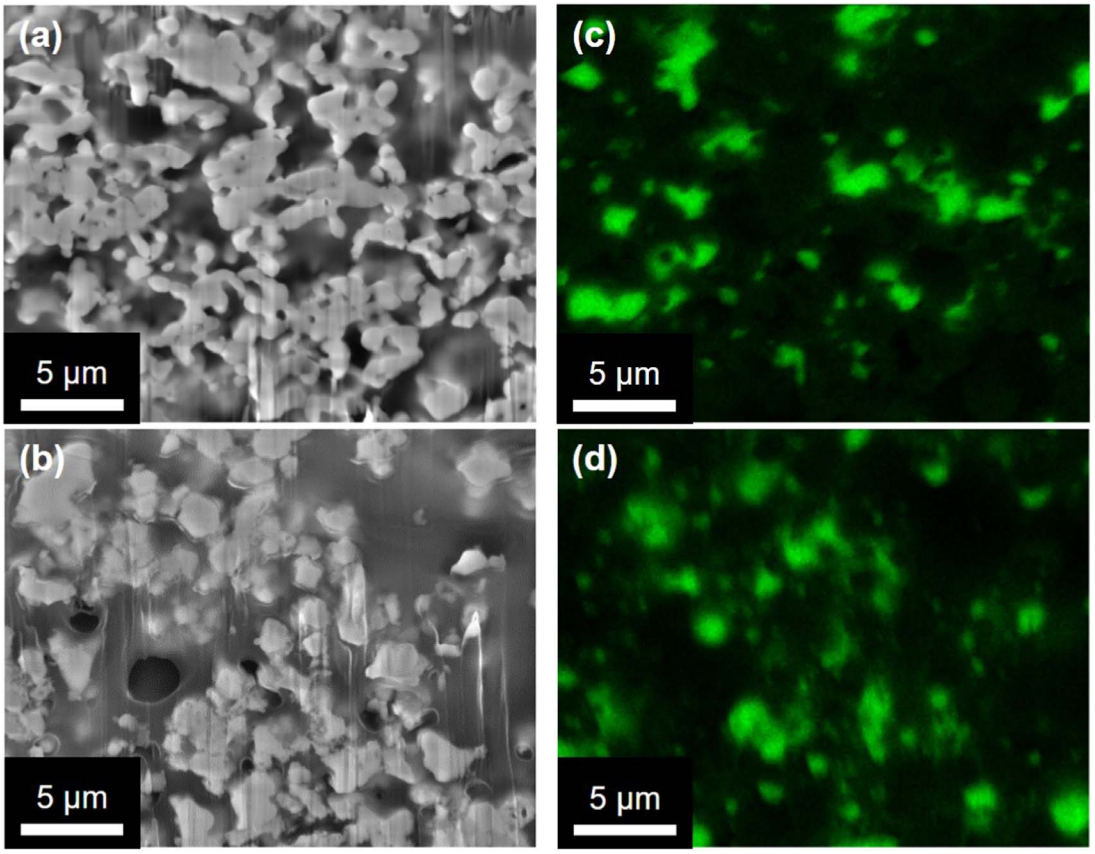

Figure 8. (a), (b) FIB-SEM micrographs and (c), (d) Ni EDS intensity maps of the $Ni_{80}Co_{20}$-GDC anode: (a), (c) before, and (b), (d) after 50 redox cycles.

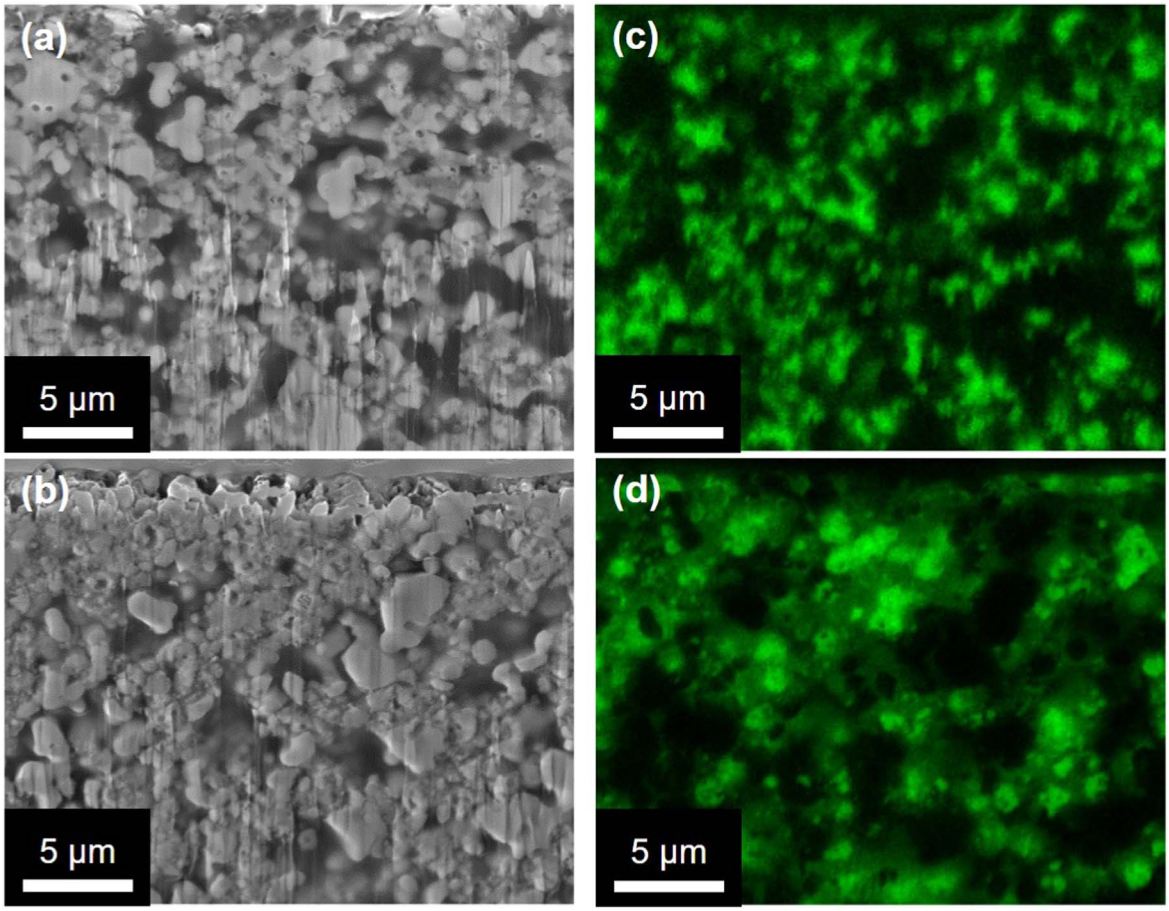

Figure 9. (a), (b) FIB-SEM micrographs and (c), (d) Ni EDS intensity maps of the $Ni_{74.5}Cr_{17.2}Fe_{8.3}$-GDC anode: (a), (c) before, and (b), (d) after 50 redox cycles.

the FIB-SEM micrographs, calculated using image analysis software. Back-scattered electron images were used to distinguish between Ni- and Ce-containing grains, based on differences in contrast due to the different atomic weights. A wet-chemical preparation procedure (Fig. 1), was applied to prepare Ni-alloy grains homogeneously mixed with GDC powders, where the Ni-containing powders were calcined at 1000 °C and the anode layers were then heat-treated at 1300 °C. Such wet-chemistry based preparation procedure is one of the reasons to obtain and maintain small Ni-based grains, even after high-temperature sintering, fuel cell operation, and redox cycling. Figure 10a reveals that the volume fraction of smaller Ni particles with diameter of 50 to 70 nm in the Ni-GDC anode is reduced from 17% to 9% after the redox cycling tests, and that the proportion of larger particles increases. This is a clear indication of Ni particle aggregation, as is often observed in conventional SOFC cermet anodes. In contrast, for the $Ni_{80}Co_{20}$-GDC and $Ni_{74.5}Cr_{17.2}Fe_{8.3}$-GDC anodes (Figs. 10b and 10c), there is a much smaller decrease in the volume fraction of 50 to 70 nm diameter particles after redox cycling (from 19% to 17%, and from 17% to 14%, respectively), and a less consistent increase in the proportion of particles with larger diameter. These quantitative results confirm that aggregation of Ni particles during redox cycling is suppressed in the Ni-alloy based cermet anodes. More detailed quantitative analysis of Ni-alloy anode microstructure is of scientific and technological relevance. Various image analysis techniques can reveal quantitative values, including porosity, phase distribution, particle size redistribution, and tortuosity. To mention a few, the tortuosity factor could quantitatively reveal the loss of contact between grains upon redox cycling. Such studies are now in progress for selected materials of interest.

In order to investigate the microstructural changes in the anodes in more detail, high-resolution STEM was used. Figure 11 shows STEM images and elemental mapping for the conventional Ni-GDC anode before and after redox cycling. Figure 12 shows similar data for the $Ni_{80}Co_{20}$-GDC anode. Figures 13 and 14 show the data for the $Ni_{74.5}Cr_{17.2}Fe_{8.3}$-GDC anode, before and after redox cycling, respectively. Figure 11b (oxygen intensity map) and 11c (nickel intensity map) indicate that Ni particles in the Ni-GDC anode are in the metallic state before redox cycling, since the oxygen and nickel distributions do not overlap. However, after redox cycling, the oxygen and nickel distributions completely overlap (Figs. 11e and 11f, respectively). This indicates that metallic Ni in the conventional Ni-GDC cermet anode is completely oxidized during the redox cycling test. Furthermore, the Ni-oxide particles appear as aggregates of multiple particles rather than spherical grains after redox cycling. These results indicate that Ni particles in the Ni-GDC anodes are repeatedly oxidized and reduced during the fuel supply and interruption cycles, causing redox-induced degradation associated with Ni aggregation.[9,25]

For the $Ni_{80}Co_{20}$-GDC anode, shown in Fig. 12, before redox cycling, the nickel and cobalt distributions overlap (Figs. 12c and 12d, respectively), confirming the formation of a homogeneous Ni–Co alloy. Furthermore, the Ni–Co alloy exists in the metallic state, since the oxygen (Fig. 12b) and nickel/cobalt distributions (Figs. 12c and 12d) do not overlap. After redox cycling, the nickel and cobalt distributions (Figs. 12g and 12h) still overlap each other, but do not overlap with the oxygen distribution (Fig. 12f), indicating that the Ni–Co alloy is not oxidized even during fuel supply interruption. Meanwhile, a clear overlap of the oxygen (Fig. 12f) and cobalt distributions (Fig. 12h) on the surface of the Ni–Co alloy

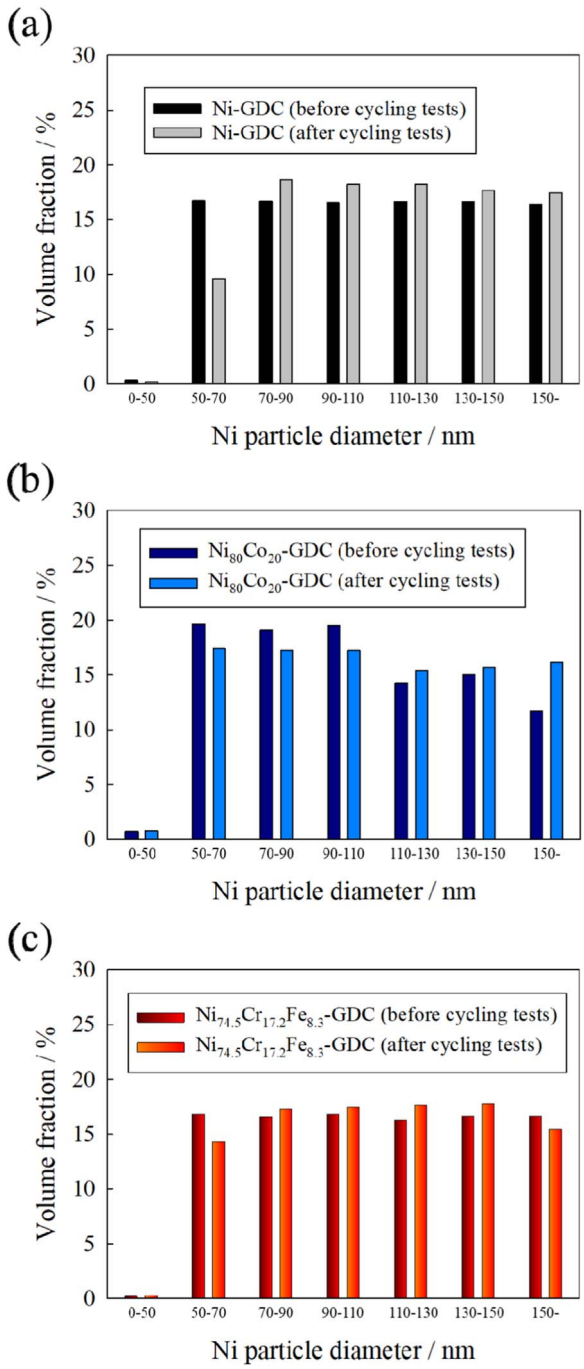

Figure 10. Ni particle size distribution for: (a) Ni-GDC anodes; (b) $Ni_{80}Co_{20}$-GDC anodes; and (c) $Ni_{74.5}Cr_{17.2}Fe_{8.3}$-GDC anodes, before and after redox cycling tests.

indicates the formation of a dense Co-rich oxide film. This layer is hypothesized to protect the metallic alloy particles from further oxidation during redox cycling. The presence of the Ni–Co alloy and the Co-rich oxide film is consistent with the thermochemical calculations (Figs. 3 and 4).

Figures 13 and 14 show the microstructure of the $Ni_{74.5}Cr_{17.2}Fe_{8.3}$-GDC anode before and after redox cycling, respectively. The nickel distribution (Fig. 13d) overlaps with the iron distribution (Fig. 13e), but only rarely overlaps with the oxygen or chromium distributions (Figs. 13c and 13f, respectively). This indicates that metallic Ni–Fe alloy is the main phase in the $Ni_{74.5}Cr_{17.2}Fe_{8.3}$-GDC anode before redox cycling. Moreover, the iron and chromium distributions overlap with the oxygen distribution (Figs. 13e, 13f, and 13c, respectively), indicating the additional presence of Fe-rich and Cr-rich oxides. After redox cycling, as shown in Fig. 14, the metallic Ni–Fe alloy is still observed to be coated with the Fe- and Cr-rich oxide layers (Figs. 14c–14f). The co-existence of these Fe-rich and Cr-rich oxides as well as the Ni–Fe alloy is consistent with the thermochemical calculations (Figs. 3 and 4). According to Fig. 3, chromium should remain in the oxidized state, while iron should be reduced in the 3%-humidified hydrogen fuel. Even after the anode was reduced at 1000 °C during the pre-treatment step, chromium remained in the oxidized state as expected, while iron could be only partially reduced due to e.g. slow reaction kinetics. In particular, Cr oxide phases are extremely stable, so only a small proportion of it is alloyed, and it mostly exists as a separate oxide phase. These Fe-rich and Cr-rich oxide layers help explain the relatively lower initial electrochemical performance, but are also

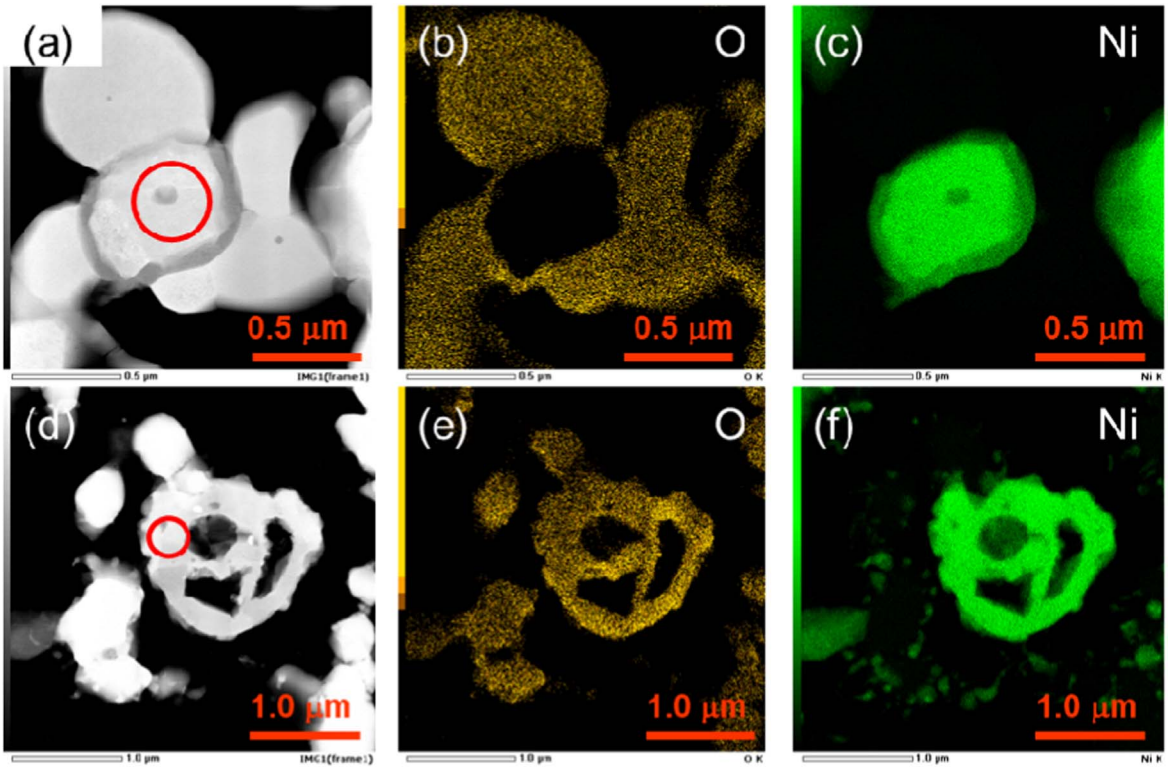

Figure 11. STEM-EDS maps for the Ni-GDC anode: (a)–(c) before; and (d)–(f) after 50 redox cycles. Red circles in the STEM images indicate areas where SAED patterns were taken in Figs. 15a and 16a.

responsible for suppressing oxidation of the Ni–Fe alloy particles during redox cycling.

More detailed microstructural observations were made via selected-area electron diffraction (SAED). Figures 15a–15c show SAED patterns for Ni-based catalyst particles in Ni-GDC, $Ni_{80}Co_{20}$-GDC, and $Ni_{74.5}Cr_{17.2}Fe_{8.3}$-GDC anodes, respectively, before redox cycling. SAED was performed at the regions highlighted by red circles in Figs. 11a, 12a, and 13a. All of the patterns corresponded to Ni-type fcc structure. This confirms that, before redox cycling, the Ni-based catalysts are pure Ni, or Ni-based alloys containing Co, Fe, or Cr as a solid solution. Lattice parameters were estimated from the diffraction spot distances, and they are all almost identical to that expected for pure Ni (0.35 nm). This may be because the atomic radii of Ni, Co, Fe, and Cr are similar.

Figures 16a–16c show SAED patterns for Ni-based particles in the Ni-GDC, $Ni_{80}Co_{20}$-GDC, and $Ni_{74.5}Cr_{17.2}Fe_{8.3}$-GDC anodes, respectively, after redox cycling. SAED was performed at the regions highlighted by red circles in Figs. 11d, 12e, and 14a. As shown in the Figs. 16b and 16c, SAED patterns for the Ni-based particles in the $Ni_{80}Co_{20}$-GDC and $Ni_{74.5}Cr_{17.2}Fe_{8.3}$-GDC anodes after redox cycling can be attributed to an fcc Ni-type structure. In contrast, the SAED patterns for Ni-based particles in the Ni-GDC anode after redox cycling (Fig. 16a) correspond to fcc NiO, with a larger lattice parameter of 0.42 nm. As such, SAED provides further evidence that Ni particles in the Ni-GDC anode are completely oxidized during redox cycling. In contrast, the oxidation of the Ni-alloy particles in the $Ni_{80}Co_{20}$-GDC and $Ni_{74.5}Cr_{17.2}Fe_{8.3}$-GDC anodes is suppressed during redox cycling.

Figures 17a and 17b respectively show a low-magnification STEM image and a high-resolution TEM (HRTEM) image for the $Ni_{80}Co_{20}$-GDC anode after redox cycling. As shown in Fig. 17a, the Ni-Co particle is coated with a Co-rich oxide layer (with slightly darker contrast). Figure 17b was taken at the region of the red square in Fig. 17a. The inset in Fig. 17b is a fast Fourier transform (FFT) of this HRTEM image. The lattice parameters correspond to NiO, and the FFT pattern is attributed to the fcc crystal structure. This confirms that the Ni–Co catalyst particle is coated with a Co-rich oxide with the same fcc type structure as NiO.

Figures 18a and 18b respectively show a low-magnification STEM image and a HRTEM image of a Ni-based catalyst particle in the $Ni_{74.5}Cr_{17.2}Fe_{8.3}$-GDC anode, before redox cycling. The insets in Fig. 18b are FFT images indicating that the inner part of the oxide exhibits an Fe_3O_4 spinel-type structure, and that the outer part exhibits a Cr_2O_3 corundum-type crystal structure. Such dense oxides could also act as the protecting layers against complete oxidation of the Ni-based grains.

Figure 19 is a schematic drawing summarizing the observed microstructural changes in pure-Ni, Ni–Co alloy, and Ni–Cr–Fe alloys used in SOFC cermet anodes, before and after redox cycling. For conventional Ni-based anodes, NiO can be formed on Ni surface. The Ni particles are completely converted to NiO under oxidizing conditions. Upon reduction to Ni, the electron conducting network is disrupted, leading to increased ohmic resistance, and therefore a degradation in electrochemical performance. In contrast, in the Ni–Co alloy anode, oxidation of the Ni–Co alloy particles is suppressed due to the formation of a protective Co-rich oxide film on the surface, preventing disruption of the electron-conducting network. In the ternary Ni–Cr–Fe alloy anode, Cr- and Fe-rich oxide phases exist even before redox cycling. Redox cycling increases the thickness of these oxides, further improving the cycling durability.

Electrode kinetics at such Ni-alloy anodes are of scientific interest. As the GDC surface itself is catalytically active,[57,58] the hydrogen oxidation reaction could occur on both Ni-alloy and GDC surfaces. Ni-alloy surfaces could act as anodic reaction sites in the same way as pure Ni surfaces, but Ni-alloys could also act as electron-conducting pathways for anodic reactions on catalytically active GDC surfaces. Fundamental electrochemical analyses are of scientific relevance for future studies, including: (i) the electrode reaction processes and catalytic activities on such Ni-alloy surfaces; (ii) the electrical conductivity and defect chemistry of related alloys

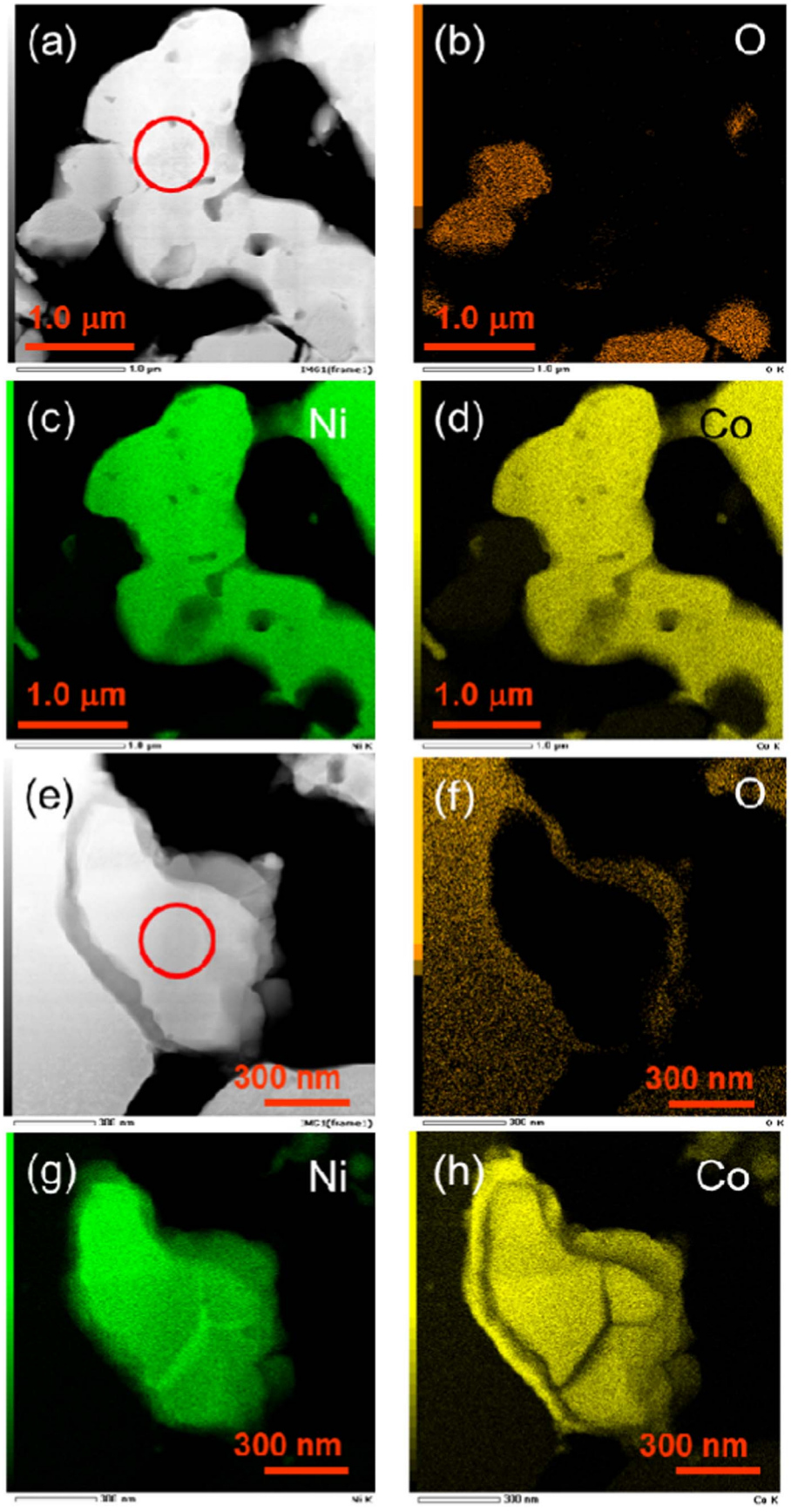

Figure 12. STEM-EDS maps of the $Ni_{80}Co_{20}$-GDC anode: (a)–(d) before; and (e)–(h) after 50 redox cycles. Red circles in the STEM images indicate the areas from which SAED patterns were taken for Figs. 15b and 16b.

and oxides in the Ni-alloy electrodes; and (iii) the role of the electrolyte component in comparison between purely ion-conducting zirconia and mixed conducting ceria in such electrodes.

It can be therefore concluded that the redox cycling durability in Ni-alloy based cermet anodes can be significantly improved by the formation of dense protective oxide film on the surfaces of the

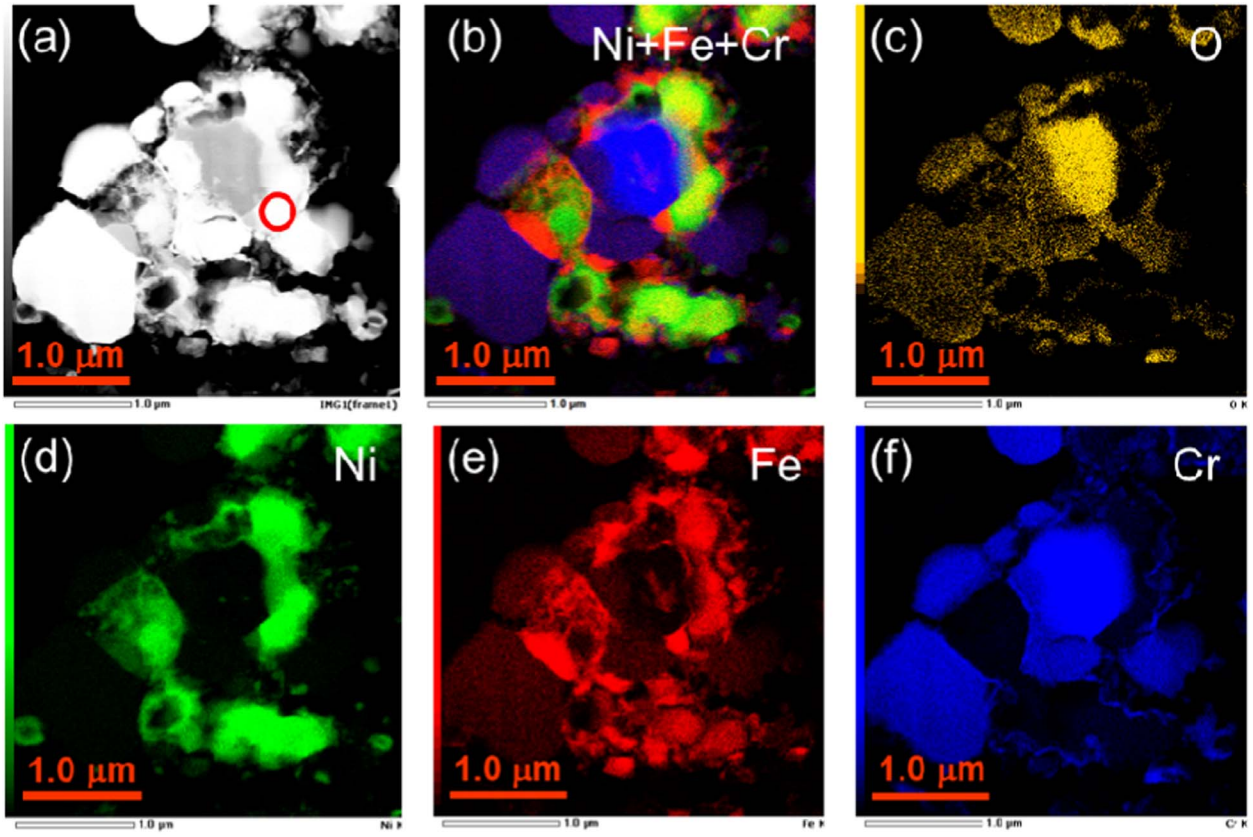

Figure 13. STEM-EDS maps for the $Ni_{74.5}Cr_{17.2}Fe_{8.3}$-GDC anode before redox cycling. The red circle in the STEM image indicates the area from which SAED patterns were taken for Fig. 15c.

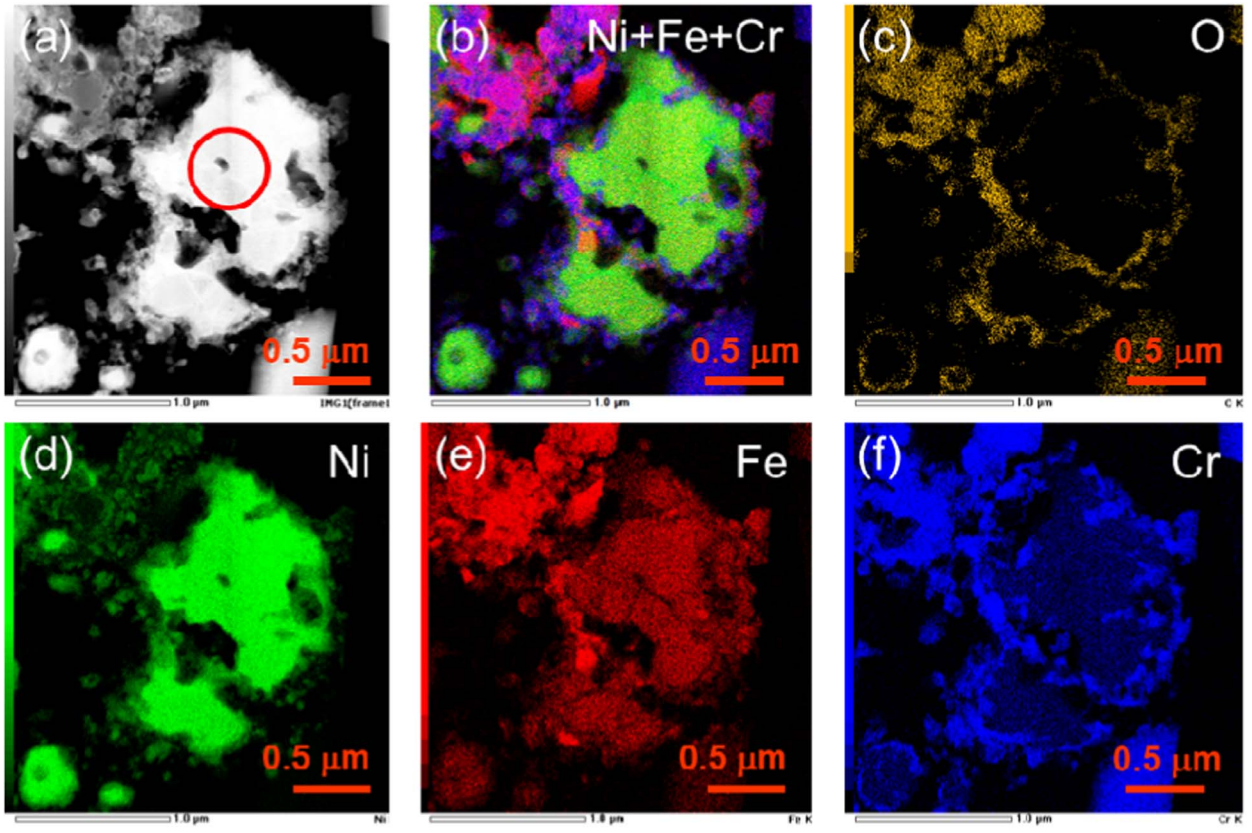

Figure 14. STEM-EDS maps for the $Ni_{74.5}Cr_{17.2}Fe_{8.3}$-GDC anode after 50 redox cycles. The red circle in the STEM image indicates the area from which SAED patterns were taken for Fig. 16c.

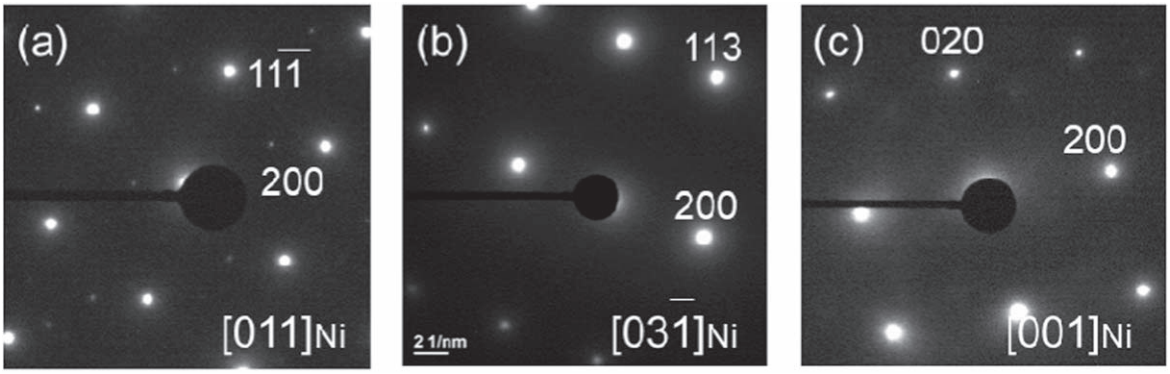

Figure 15. Selected-area electron diffraction (SAED) patterns of Ni-based catalyst particles in: (a) the Ni-GDC anode; (b) the $Ni_{80}Co_{20}$-GDC anode; and (c) the $Ni_{74.5}Cr_{17.2}Fe_{8.3}$-GDC anode, before redox cycling. All of the SAED patterns are attributed to the Ni-type FCC crystal structure. These SAED patterns were observed from the zone axes of [011], [03$\bar{1}$] and [001], respectively.

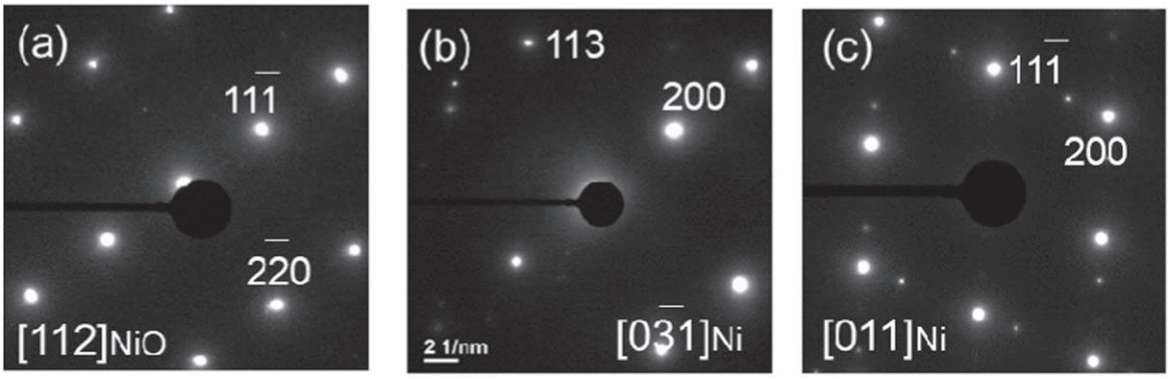

Figure 16. Selected area electron diffraction (SAED) patterns of Ni-based catalyst particles in: (a) the Ni-GDC anode; (b) the $Ni_{80}Co_{20}$-GDC anode; and (c) the $Ni_{74.5}Cr_{17.2}Fe_{8.3}$-GDC anode after 50 redox cycles.

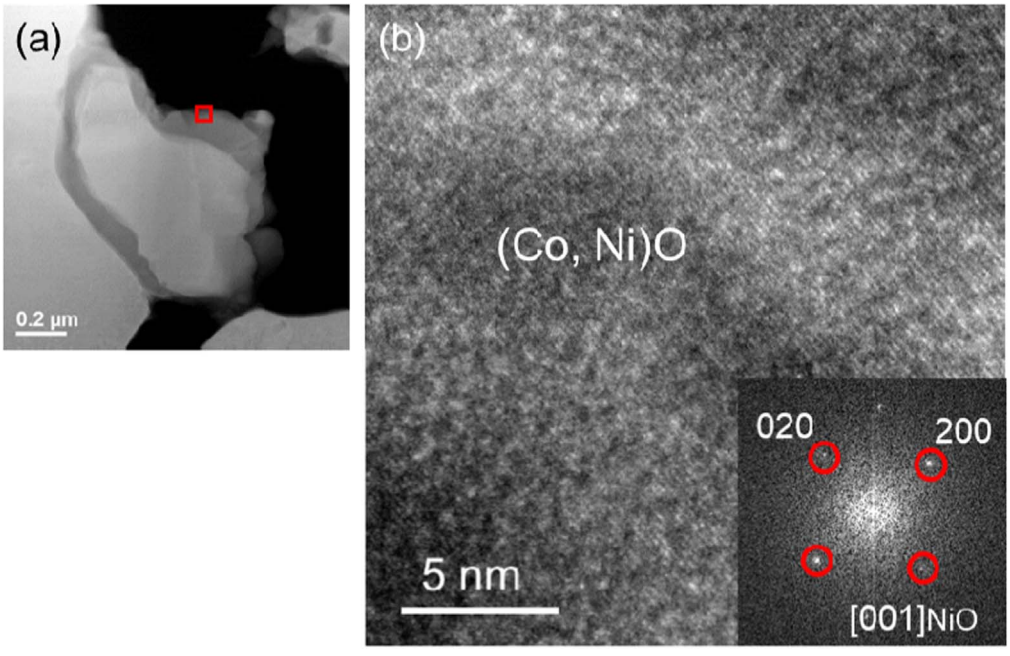

Figure 17. (a) Low-magnification STEM image, and (b) high-resolution TEM image of the region highlighted by a red square in (a), with fast Fourier transform (FFT) *(inset)*. These images were taken at the surface of the Ni-based catalyst particle in the $Ni_{80}Co_{20}$-GDC anode, after 50 redox cycles.

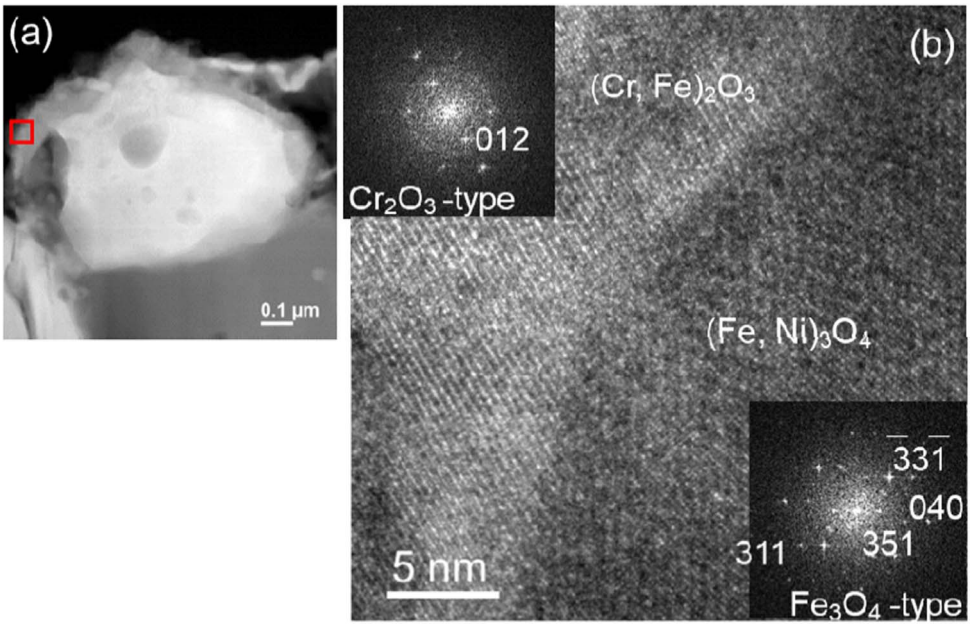

Figure 18. (a) Low-magnification STEM image, and (b) high-resolution TEM image of the region highlighted by a red square in (a), with fast Fourier transform (FFT) *(inset)*. Images were taken at the surface of the Ni-based catalyst in the $Ni_{74.5}Cr_{17.2}Fe_{8.3}$-GDC anode, before redox cycling.

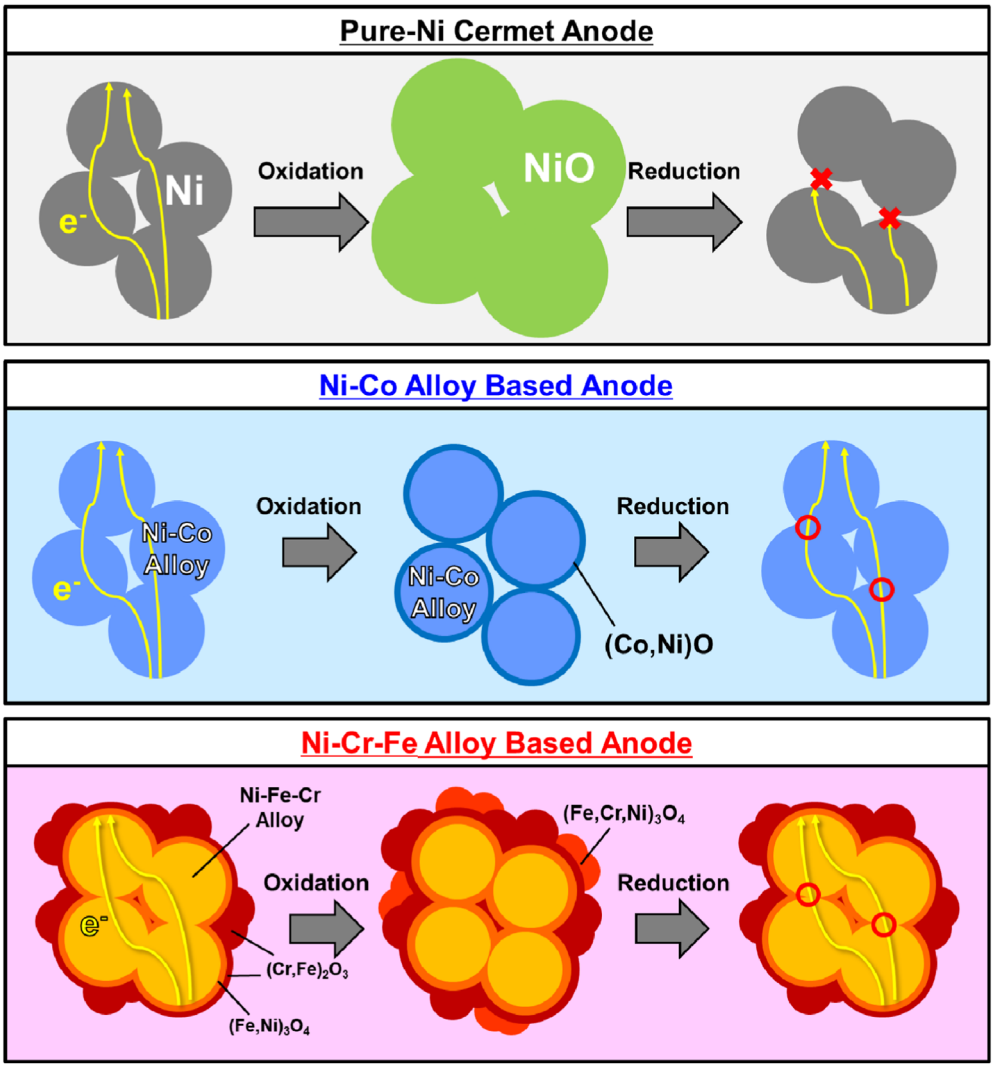

Figure 19. Schematic drawing of the microstructural changes of pure-Ni, Ni–Co alloy, and Ni–Cr–Fe alloys in SOFC cermet anodes, before and after redox cycling.

Ni-based alloy catalyst particles. This suppresses complete oxidation of the catalyst particles, preventing changes in the volume and the associated disruption of the electron-conducting network in SOFC anodes.

Conclusions

Ni-alloy cermet anodes were developed which significantly suppressed redox-induced degradation of SOFCs. The Ni-alloy based cermet anodes consisted of Ni, Co, Fe, and/or Cr. In particular, the $Ni_{80}Co_{20}$-GDC alloy anode is thermochemically stable within a wide humidification range even beyond 80% (i.e. up to a high fuel utilization beyond ca. 80%) in hydrogen-containing fuels, and exhibited comparable initial electrochemical performance with the conventional Ni-GDC anode. The Ni-alloy based anodes exhibited higher redox stability compared with conventional anodes. Microstructural observation indicated that aggregation of the Ni particles during redox cycling was suppressed. High-resolution electron microscopy revealed Co-rich oxides on surface of the Ni–Co alloy catalyst particles, Fe-rich oxides on the Ni–Fe alloy catalyst particles, and Cr-rich/Fe-rich oxides on the surface of Ni–Cr–Fe alloy catalyst particles. These oxide layers provide a protective coating to the catalyst particles, preventing the volume change associated with oxidation, and thereby suppressing disruption of the electron-conducting network during redox cycling. The Ni-alloy based cermet anodes prepared in this study can exhibit comparable initial electrochemical performance to conventional Ni-based cermet anodes in SOFCs, as well as significantly improved redox stability. The use of such redox-stable anodes will potentially improve the robustness of SOFC anodes and simplify the control of SOFC systems by eliminating the inert and/or reducing gas flow currently required to protect conventional Ni cermet anodes.

Acknowledgments

This work was supported by Japan Science and Technology Agency (JST) through the 'Center of Innovation Science and Technology based Radical Innovation and Entrepreneurship Program (COI Program, grant no. JPMJCE1318)'. We also thank Mr Katsuya Natsukoshi in Kyushu University for evaluating experimental data.

ORCID

Shunsuke Taniguchi https://orcid.org/0000-0001-6661-7618
Kazunari Sasaki https://orcid.org/0000-0002-3174-9087

References

1. N. Q. Minh, *J. Am. Ceram. Soc.*, **76**, 563 (1993).
2. B. C. H. Steele and A. Heinzel, *Nature*, **414**, 45 (2001).
3. S. C. Singhal and K. Kendall, *High Temperature Solid Oxide Fuel Cells*, ed. S. C. Singhal and K. Kendall (Elsevier, Amsterdam) (2003).
4. J. Larminie and A. Dicks, *Fuel Cell Systems Explained* (Wiley, England) 2nd ed. (2003).
5. W. Vielstich, A. Lamm, and H. A. Gasteiger, *Handbook of Fuel Cells: Fundamentals, Technology, and Applications* (Wiley, New York) (2003).
6. K. Sasaki, H.-W. Li, A. Hayashi, J. Yamabe, T. Ogura, and S. M. Lyth, *Hydrogen Energy Engineering: A Japanese Perspective* (Springer, Japan) (2016).
7. EneFarm Partners, Press Release, Tokyo Japan, November 21 (2019), https://gas.or.jp/user/comfortable-life/enefarm-partners/ (in Japanese), (accessed 2020. 6. 14).
8. Y. Matsuzaki, Y. Tachikawa, T. Somekawa, T. Hatae, H. Matsunoto, S. Taniguchi, and K. Sasaki, *Sci. Rep.*, **5**, 12640 (2015).
9. J. Matsuda, T. Kawasaki, S. Futamura, T. Kawabata, S. Taniguchi, and K. Sasaki, *Microscopy*, **67**, 251 (2018).
10. W. Bujalski, J. Paragreen, G. Reade, S. Pyke, and K. Kendall, *J. Power Sources*, **157**, 745 (2006).
11. W. Bujalski, C. M. Dikwal, and K. Kendall, *J. Power Sources*, **171**, 96 (2007).
12. Y. Guan et al., *J. Power Sources*, **196**, 10601 (2011).
13. N. Takagi, N. Shikazono, and N. Kasagi, *Proc. JSME Annual Meeting* (The Japan Society of Mechanical Engineers, Morioka Japan) p. 119 (2009).
14. T. Werber, *Solid State Ionics*, **42**, 205 (1990).
15. D. Waldbilling, A. Wood, and D. G. Ivey, *J. Power Sources*, **145**, 206 (2005).
16. B. Liu, Y. Zhang, B. Tu, Y. Dong, and M. Cheng, *J. Power Sources*, **165**, 114 (2007).
17. K. Fujita, T. Somekawa, K. Horiuchi, and Y. Matsuzaki, *J. Power Sources*, **193**, 130 (2009).
18. J. Laurencin, G. Delette, O. Sicardy, S. Rosini, and F. Lefebvre-Joud, *J. Power Sources*, **195**, 2747 (2010).
19. Q. Jeangros, A. Faes, J. B. Wagner, T. W. Hansen, U. Aschauer, J. van Herle, A. Hessler-Wyser, and R. E. Duni-Borkowski, *Acta Mater.*, **58**, 4578 (2010).
20. H. Sumi, R. Kishida, J. Kim, H. Muroyama, T. Matsui, and K. Eguchi, *J. Electrochem. Soc.*, **157**, B1747 (2010).
21. M. H. Pihlatie, A. Kaiser, M. Mogensen, and M. Chen, *Solid State Ionics*, **189**, 82 (2011).
22. L. Holzer et al., *J. Power Sources*, **196**, 1279 (2011).
23. L. Holzer, B. Iwanschitz, T. Hocker, L. Keller, O. Pecgo, G. Sartoris, P. Gasser, and B. Muench, *J. Power Sources*, **242**, 179 (2013).
24. K. Sasaki, S. Adachi, K. Haga, M. Uchikawa, J. Yamamoto, A. Iyoshi, J. T. Chou, Y. Shiratori, and K. Itoh, *ECS Trans.*, **7**, 1675 (2007).
25. T. Kawasaki, J. Matsuda, Y. Tachikawa, S. M. Lyth, Y. Shiratori, S. Taniguchi, and K. Sasaki, *Int. J. Hydrogen Energy*, **44**, 9386 (2019).
26. Q. Fang, L. Blum, R. Peters, M. Peksen, P. Batfalsky, and D. Stolten, *Int. J. Hydrogen Energy*, **40**, 1128 (2015).
27. M. Hanasaki, C. Uryu, T. Daio, T. Kawabata, Y. Tachikawa, S. M. Lyth, Y. Shiratori, S. Taniguchi, and K. Sasaki, *J. Electrochem. Soc.*, **161**, F850 (2014).
28. X. Shen and K. Sasaki, *J. Power Sources*, **320**, 180 (2016).
29. X. Shen and K. Sasaki, *Int. J. Hydrogen Energy*, **41**, 17044 (2016).
30. X. Shen, T. Chen, S. R. Bishop, N. H. Perry, H. L. Tuller, and K. Sasaki, *J. Power Sources*, **370**, 122 (2017).
31. S. Futamura, Y. Tachikawa, J. Matsuda, S. M. Lyth, Y. Shiratori, S. Taniguchi, and K. Sasaki, *J. Electrochem. Soc.*, **164**, F3055 (2017).
32. S. Futamura, A. Muramoto, Y. Tachikawa, J. Matsuda, S. M. Lyth, Y. Shiratori, S. Taniguchi, and K. Sasaki, *Int. J. Hydrogen Energy*, **44**, 8502 (2019).
33. Z. Wang and M. Mori, *J. Fuel Cell Sci. Technol.*, **8**, 051018 (2011).
34. Z. Wang, M. Mori, and T. Itoh, *J. Electrochem. Soc.*, **157**, B1783 (2010).
35. O. A. Marina, N. L. Canfield, and J. W. Stevenson, *Solid State Ionics*, **149**, 21 (2002).
36. X. Sun, S. Wang, Z. Wang, X. Ye, T. Wen, and F. Huang, *J. Power Sources*, **183**, 114 (2008).
37. K. B. Yoo and G. M. Choi, *Solid State Ionics*, **192**, 515 (2011).
38. K. B. Yoo and G. M. Choi, *Solid State Ionics*, **180**, 867 (2009).
39. G. Chen, H. Kishimoto, K. Yamaji, K. Kuramoto, and T. Horita, *J. Electrochem. Soc.*, **162**, F223 (2015).
40. M. R. Pillai, I. Kim, D. M. Bierschenk, and S. A. Barnett, *J. Power Sources*, **185**, 1086 (2008).
41. C. Kittel, *Introduction to Solid State Physics* (Wiley, New York) 8th ed. (2004).
42. K. Araki, J. Yamamoto, Y. Shiratori, K. Ito, and K. Sasaki, *ECS Trans.*, **25**, 2039 (2009).
43. Scientific Group Thermodata Europe (SGTE), "Thermodynamic properties of inorganic materials." *Landolt-Börnstein Group IV (Physical Chemistry)* (Springer-Verlag, Berlin-Heidelberg) Vol. 19 (2001).
44. G. Belov, V. Iorish, and V. Yungman, *Calphad*, **23**, 173 (1999).
45. I. Barin, *Thermochemical Data of Pure Substances* (VCH Verlags Gesellschaft, Weinheim, Germany) (1989).
46. P. Patnaik, *Handbook of Inorganic Chemicals* (McGraw-Hill, New York) (2003).
47. M. W. Chase Jr, "NIST-JANAF, thermochemical tables - fourth edition." *J. Phys. Chem. Ref. Data*, Mononograph No. 9 (1998).
48. M. W. Chase, C. A. Daives, J. R. Downey, D. J. Frurip, R. A. McDonald, and A. N. Syverud, "JANAF thermochemical tables - third edition." *J. Phys. Chem. Ref. Data*, **14**, 927 (1985).
49. K. Sasaki, J. P. Wurth, R. Gschwend, M. Gödickemeier, and L. J. Gauckler, *J. Electrochem. Soc.*, **143**, 30 (1996).
50. S. B. Adler, *J. Electrochem. Soc.*, **149**, E166 (2002).
51. M. Cimenti, A. C. Co, V. I. Birss, and J. M. Hill, *Fuel Cells*, **7**, 364 (2007).
52. F. D. Richardson and J. H. E. Jeffes, *J. Iron Steel Inst.*, **160**, 261 (1948).
53. L. S. Darken and R. W. Gurry, *Physical Chemistry of Metals* (McGraw-Hill Book Company, New York) (1953).
54. W. D. Kingery, H. K. Bowen, and D. R. Uhlmann, *Introduction to Ceramics* (John Wiley & Sons, New York) 2nd ed. (1976).
55. J. Larminie and A. Dicks, *Fuel Cell Systems Explained* (John Wiley & Sons, West Sussex, England) 2nd ed. (2003).
56. W. L. Bragg, *Nature*, **128**, 511 (1931).
57. W. C. Chueh, Y. Hao, W. Jung, and S. M. Haile, *Nat. Mater.*, **11**, 155 (2012).
58. A. Nenning, C. Bischof, J. Fleig, M. Bram, and A. K. Opitz, *Energies*, **13**, 987 (2020).